AFRL-MN-EG-TR-2001-7104

EXPERIMENTAL AND COMPUTATIONAL RESULTS OF A MANEUVERABLE POWER-LAW ELLIPTIC CROSS-SECTION PROJECTILE AT SUPERSONIC SPEEDS

Gregg Abate
AFRL/MNAV
Eglin AFB, Florida 32542

John J. Bertin
Captain James R. Forsythe
Paul H. Schuricht
US Air Force Academy, CO 80840

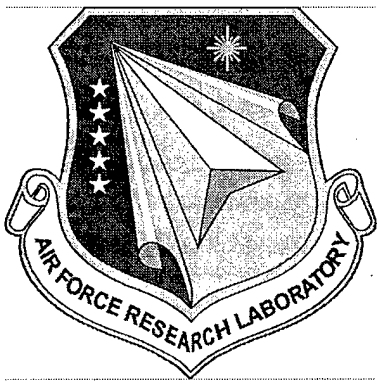

Occtober 2001

FINAL REPORT FOR PERIOD JANUARY 1998 to AUGUST 2001

DISTRIBUTION A: Approved for public release; distribution unlimited.

AIR FORCE RESEARCH LABORATORY, MUNITIONS DIRECTORATE
Air Force Material Command ■ United States Air Force ■ Eglin Air Force Base

NOTICE

When Government drawings, specifications, or other data are used for any purpose other than in connection with a definitely Government-related procurement, the United States Government incurs no responsibility or any obligation whatsoever. The fact that the Government may have formulated or in any way supplied the said drawings, specifications, or other data, is not to be regarded by implication, or otherwise in any manner construed, as licensing the holder, or any other person or corporation; or as conveying any rights or permission to manufacture, use, or sell any patented invention that may in any way be related thereto.

This technical report is releasable to the National Technical Information Services (NTIS). At NTIS it will be available to the general public, including foreign nations.

This technical report has been reviewed and is approved for publication.

FREDERICK A. DAVIS
Technical Director
Assessment and Demonstrations Division

GREGG ABATE
Program Manager
Flight Vehicles Integration Branch

Anyone having need for a copy of this report should first contact the Defense Technical Information Center (DTIC) at the address shown below. If you are a registered DTIC User, DTIC can provide you with a copy. Please do not request copies from the Air Force Research Laboratory, Munitions Directorate. Requests for additional copies should be directed to:

Defense Technical Information Center (DTIC)
8725 John J. Kingman Road, Ste 0944
Ft Belvoir, VA 22060-6218

This report is published in the interest of the scientific and technical information exchange. Publication of this report does not constitute approval or disapproval of the ideas or findings.

If your address has changed, if you wish to be removed from our mailing list, or if your organization no longer employs the addressee, please notify AFRL/MNAV, 101 W. Eglin Blvd., Suite 332, Eglin AFB FL 32542-6810, to help us maintain a current mailing list.

Do not return copies of this report unless contractual obligations or notice on a specific document requires that it be returned.

REPORT DOCUMENTATION PAGE

Form Approved
OMB No. 0704-0188

1. AGENCY USE ONLY *(Leave blank)*	2. REPORT DATE	3. REPORT TYPE AND DATES COVERED
	October 2001	Final Report January 1998 – August 2001

4. TITLE AND SUBTITLE
EXPERIMENTAL AND COMPUTATIONAL RESULTS OF A MANEUVERABLE POWER-LAW ELLIPTIC CROSS-SECTION PROJECTILE AT SUPERSONIC SPEEDS

5. FUNDING NUMBERS
JON: 2303PR81

PE: 61102F
PR: 2303
TA: PR
WU: 81

6. AUTHOR(S)
Gregg Abate (AFRL/MNAV), John J. Bertin (USAFA), James R. Forsythe (USAFA), and Paul H. Schuricht (USAFA)

7. PERFORMING ORGANIZATION NAME(S) AND ADDRESS(ES)
Air Force Research Laboratory Munitions Directorate
Assessment and Demonstrations Division
Flight Vehicles Integration Branch (AFRL/MNAV), Eglin AFB FL 32542-6810

United States Air Force Academy
Department of Aeronautics
USAFA, CO 80840

8. PERFORMING ORGANIZATION REPORT NUMBER

9. SPONSORING/MONITORING AGENCY NAME(S) AND ADDRESS(ES)
Air Force Research Laboratory Munitions Directorate
Assessment and Demonstrations Division
Flight Vehicles Integration Branch (AFRL/MNAV), Eglin AFB FL 32542-6810
POC: Gregg Abate, 850 882 4085

10. SPONSORING/MONITORING AGENCY REPORT NUMBER
AFRL-MN-EG-TR-2001-7104

11. SUPPLEMENTARY NOTES
Availability of report is specified on front cover

12a. DISTRIBUTION/AVAILABILITY STATEMENT
DISTRIBUTION A: Approved for public release; distribution unlimited

12b. DISTRIBUTION CODE

13. ABSTRACT *(Maximum 200 words)*
This report documents the results of an experimental and computational investigation of a power-law elliptic cross-section projectile for increased maneuverability. Surface-pressure measurements and force-and-moment measurements have been conducted in the Tri-Sonic Wind-Tunnel (TWT) at the Aerodynamic Research Center (ARC) at the U.S. Air Force Academy. Flow visualization data were also obtained in the form of Schlieren photographs and surface oil-flow patterns during these test programs. Data were obtained at a Mach number of 4.28 over a range of Reynolds numbers (based on the free-stream conditions and the model length) of 12.47 million to 19.96 million over an angle-of-attack range from -11 to +11 degrees. The data from these wind-tunnel tests were compared with computations generated using the Cobalt code, which was run on the Beowulf cluster at the High-Performance Computing Facility (HPCF) at the ARC. It should be noted that the experimental and the computational parts of this investigation were conducted concurrently in a double-blind fashion. That is, the results from the experimental effort were not used to influence the way in which the results from the CFD effort were produced and vice versa. Free flight investigations were carried out at the U.S. Air Force Research Laboratory Munitions Directorate Aeroballistic Research Facility and were conducted at Mach numbers ranging from 3.0 to 5.0. The free flight experimental data consisted of nine free-flight projectiles launched within an instrumented facility. Additional computational work was again carried out via the Cobalt code at the flight conditions of the experimental facility. The results indicate good agreement between the experimental and computational data determined in this effort, as well as, with engineering level predictions. The free-flight data was limited to small angles of attack therefore high fidelity determination of the aerodynamic stability coefficients and derivatives was not possible. Discrepancies were seen in the center of pressure data between the experimental and the computational data and require further investigation.

14. SUBJECT TERM
Elliptic Bodies, Non-Circular Cross Section, Experimental Aerodynamics, Spark range tests, Trajectory analysis, Aerodynamics, Cobalt, CFD, Wind Tunnel Testing

15. NUMBER OF PAGES
76

16. PRICE CODE

17. SECURITY CLASSIFICATION OF REPORT	18. SECURITY CLASSIFICATION OF THIS PAGE	19. SECURITY CLASSIFICATION OF ABSTRACT	20. LIMITATION OF ABSTRACT
UNCLASSIFIED	UNCLASSIFIED	UNCLASSIFIED	UL

NSN 7540-01-280-5500

Standard Form 298 (Rev. 2-89)
Prescribed by ANSI Std. 239-18

INTENTIONALLY LEFT BLANK

PREFACE

This report documents the aerodynamic characteristics of a power-law elliptic cross-section configuration. This effort consisted of wind tunnel tests and free flight aeroballistic tests. Complementary numerical modeling and simulation was performed to match both of these experimental data sets.

The free flight tests were conducted in the USAF Aeroballistic Research Facility, located at Eglin AFB, FL. The data analysis was accomplished by the Arrow Tech Associates of South Burlington, Vermont 05401-4985, under Contract F08630-96-C-0001, with the Air Force Research Laboratory Munitions Directorate, Eglin Air Force Base, Florida 32542-5434. Gregg Abate was the principal investigator and test director. Mr. John Krieger conducted the tests that included launch, instrumentation, data acquisition, and image processing.

The wind tunnel tests were conduced at the United States Air Force Academy under the direction of Dr. John Bertin. Mr. Larry Lamblin was the Director of Tri-Sonic Tunnel Operations and Mr. Bobby Hatfield was the craftsman who built and instrumented the models. Special thanks go to Tim Hayden and to SSgt Buddy Johns who provided the software support to facilitate the ever-changing data-reduction needs for the experimental program.

The numerical analysis was performed by Capt. James Forsythe of the United States Air Force Academy.

INTENTIONALLY LEFT BLANK

TABLE OF CONTENTS

page

PREFACE v

LIST OF FIGURES ix

LIST OF TABLES xi

I INTRODUCTION 1

1. Background 1
2. Research Shape 4

II WIND TUNNEL TESTING 5

1. Wind Tunnel Test Facility 5
2. Test Conditions 6
3. Wind Tunnel Test Models 7

III AEROBALLISTIC TESTING 13

1. Free Flight Facility 13
2. Free Flight Model Design 13
3. Free Flight Test Conditions 15
4. Aerodynamic Predictions 16

IV COMPUTATIONAL ANALYSIS 17

1. Solutions of Wind Tunnel Data 17
2. Solutions of Free Flight Data 18

V RESULTS AND DISCUSSION 21

1. Wind Tunnel Data 21
2. Free Flight Data 44

VI CONCLUSIONS 49

1. Wind Tunnel Data 49
2. Free Flight Data 50

APPENDIX A – NOMENCLATURE 51

APPENDIX B – BODY FIXED AERODYNAMIC MODEL 55

1. 6DOF – Methodology 55
2. Aerodynamic Forces and Moments 57

REFERENCES 61

THIS PAGE INTENTIONALLY LEFT BLANK

LIST OF FIGURES

Figure page

1. H3 model geometry 4
2. Schematic of USAF Academy Tri-Sonic Wind Tunnel 5
3. USAFA Tri-Sonic Wind Tunnel performance envelope 6
4. Configuration geometry and coordinate system for slender, power-law elliptic-section model 8
5. The models tested, from left to right: APM, APB, EPB 8
6. Location of the surface pressure ports for the APB and EPB models 9
7. Location of the surface pressure ports for the APM model 10
8. Free-flight ballistic range model 14
9. Free-flight model sabot 14
10. ARFDAS parameter identification process 16
11. $Cobalt_{60}$ unstructured grid generated by VGRIDns for 0° angle of attack 18
12. Detail of $Cobalt_{60}$ grid near the nose 18
13. Computational domain for the alpha cases 19
14. Grid close-up view of the base region for the zero degree cases 19
15. CFD results for zero alpha, Mach 4.2, free-flight conditions - surface colored by pressure, Schlieren on the symmetry plane, and streamlines in the base region 20
16. $Cobalt_{60}$ calculated Mach contours 22
17. $Cobalt_{60}$ calculated Mach contours 23
18. The bow shock wave at $\alpha = 0^{\circ}$ 24
19. Bow shock wave angle measurements 25
20. Pressure measurements illustrating the repeatability of the data for $\alpha = 0$ and $P_{tl} = 175$ *psia* 26
21. The effect of Reynolds number on the spanwise pressure distribution for $\alpha = 0^{\circ}$ 28
22. Comparison of pressures at 0° for the APM model with CFD 28
23. Vector components of the velocity in planes of constant x (cross-section planes) 30
24. Surface pressures for the APB and EPB models at $\alpha = 6^{\circ}$ 31
25. Surface pressures for the APM model at $\alpha = 6^{\circ}$ 31

26. Schlieren photographs for the flowfield for the baseline configuration at an angle of attack of ± *6°*, P_{t1} = *175 psia* 32
27. $Cobalt_{60}$ results at $\alpha = 11°$ 33
28. Oil flow patterns at $\alpha = 10°$ 34
29. Primary and secondary separation locations at $\alpha = 11°$ 34
30. Experimental and computational Schlieren images at $\alpha = 11°$ 36
31. Computational flowfield using Schlieren option for $\alpha = 11°$ with streamlines added 37
32. Surface pressures for the APB and EPB models at $\alpha = 11°$ 37
33. Schlieren photographs for the flowfield for the baseline configuration at an angle of attack of ± *11°*, P_{t1} = *175 psia* 39
34. Normal force for an H3 model 40
35. Effective axial force for an H3 model 41
36. Pitching moment coefficient around the apex for the AFB model as a function of alpha 43
37. The location of the center of pressure as a function of alpha 44
38. Zero-yaw axial force coefficient vs. Mach number 46
39. Pitch plane normal force coefficient derivative vs. Mach number 46
40. Yaw plane normal force coefficient derivative vs. Mach number 47
41. Pitch plane moment coefficient derivative vs. Mach number 47
42. Yaw plane moment coefficient derivative vs. Mach number 47
43. Center of pressure variation vs. Mach number 47
44 Shadowgraph of H3 projectile traveling at Mach 3.32 (shot 67) 47

LIST OF TABLES

Table page

1. Correlation between the stagnation chamber pressure and the free-stream Reynolds number based on model length of 12.00 inches for the nominal test conditions of the present program 7
2. The nomenclature and the dimensions of the models for which data relevant to the present report were obtained 8
3. Locations of the static pressure orifices for the EPB and APB models. 10
4. Locations of the static pressure orifices for APM model. 10
5. Free Flight Model Physical Properties 14
6. Slope of the baseline-model surface in the pitch plane (dz/dx) and in the yaw plane (dy/dx) 27
7. Aerodynamic Results 45

THIS PAGE INTENTIONALLY LEFT BLANK

SECTION I

INTRODUCTION

1. Background

Maneuverable, high-energy projectiles that can be launched either from stationary guns or from mobile guns have the potential to enhance significantly the military effectiveness of the weapons system. Applications (both offensive and defensive) include air-to-air, air-to-surface, surface-to-air, and surface-to-surface scenarios. Non-conventional configurations offer the possibility of generating larger amounts of lift than would be produced by configurations with an axi-symmetric cross-section. Hence, they are potentially more maneuverable. Examples of such non-conventional configurations are (one-half)-power-law elliptic-section (PLES) configurations. (One-half)-power-law elliptic-section configurations not only produce relatively large amounts of lift, but they are also more amenable to the blunting that is required to limit the severity of the aerodynamic heating to the vehicle surface in the vicinity of the stagnation point. Another advantage of elliptic-section bodies is the relatively small perturbation to the flow field when compared to those for conventional cone-cylinder-flare configurations. As a result, the design for launchability is made easier.

The United States Air Force Research Laboratory Munitions Directorate (AFRL/MN) is part of an international effort to develop enhanced capabilities to predict the aerodynamics of future, advanced hypersonic systems, such as those described in the previous paragraph. The design process makes complementary use of experimental programs and of analytical/numerical methods of varying degree of rigor. Although the geometry for PLES configurations is relatively simple, the subsequent discussion will demonstrate that the flow fields contain subtle complexities. Thus, it is important that the wind-tunnel tests and the computational algorithms used in the design process properly model the flow physics.

Experimental data were obtained on right-elliptic cones and on (one-half)-power-law elliptic-section cones in a Mach 8.2 air-stream in the Cranfield University Hypersonic Gun Tunnel[1]. Schlieren photographs were used to define the shape of the shock wave for the right-elliptic cone. Kontis et al.[1] noted: "The distance between the shock wave and the body, for 0° incidence, is greater in the meridian plane containing the minor axis than in the meridian containing the major axis. The shock wave is not an ellipse similar to the body, but is `pushed in' toward the major axis and `pulled out' from the minor axis. This shape is because of the presence of a cross flow from the high pressure sides at the ends of the major axis to the low pressure sides at the ends of the minor axis."

Oil-flow patterns that were obtained during the present program indicated that, even at relatively low angles-of-attack, boundary-layer separation occurred as the air flowed from the windward surface, around the relatively sharp change in cross section

that occurs near the yaw plane. The free-vortex type of separation contained supersonic helical vortices that coalesced in the leeward plane-of-symmetry[2]. The recirculating, helical vortical flow impinged on the surface, creating an attachment line in the leeward plane-of-symmetry. The reattaching vortex pair produced a feather pattern in the oil film on the leeward surface of the model as the recirculating flow proceeded downstream and away from the leeward plane-of-symmetry. The oil-flow patterns obtained during the present program with the PLES model at an angle-of-attack of 10° indicated that a second, imbedded free-vortex-type separation occurred long before the recirculating flow reached the yaw plane. Thus, even for relatively small angles-of-attack, the flow field around the elliptic cross-section contained both primary and secondary separation streamlines.

Based on surface oil-flow patterns, Kontis et al.[1] also concluded that: "The flow separates on the leeward side of the body to form a pair of counter rotating vortices at low incidence for all models tested. The vortices grow with incidence."

An experimental program has been conducted by Pagan et al.[3] to develop an understanding of the vortical structures that form when boundary-layer separation occurs at moderate or high angles-of-attack. The experimental investigation of the flow field for an ogive cylinder at supersonic free-stream Mach numbers focused on the influences both of incidence and of turbulence. At low-to-moderate incidences (up to 10°), the flow structure included a primary cross-flow separation and a secondary cross-flow separation. As a result, the flow field contained both a primary and a secondary vortex. Pagan et al.[3] found that the influence of turbulence was strongest at low incidence.

For the conceptual design phase, reasonable estimates of the aerodynamic characteristics of the configuration may be made with aeroprediction codes that make considerable use of semempirical techniques[4] or of relatively simple analytical techniques[5]. The comments made in the previous paragraphs indicate that, even though the configuration geometry is simple, the flow fields for PLES configurations contain some subtle complexities. Kontis et al.[6] noted: "in the conceptual design phase, a simple description of the aerodynamic characteristics is sufficient to assess candidate configurations. As the development process carries on, the complexity and detail required increases and the source of data changes, from an almost exclusive reliance on engineering prediction methods, to a high dependence on results from detailed wind tunnel tests. There are obvious advantages in being able to proceed further with weapons development before limitations of available prediction methods force the designer to resort to expensive and time-consuming wind tunnel tests. In recent years an increasing number of new weapon designs have included features, such as non-circular cross-sectional bodies, air intakes, or novel control concepts, which cannot usually be addressed using engineering prediction methods."

Grasso and Iaccarino[7] state: "Numerical simulations may suffer from a lack of understanding of the controlling phenomena and/or inappropriate physical models, as well as limited experimental information." Grasso and Iaccarino[7] noted further that: "at high incidence and even for (geometrically simple) slender bodies, in the leeside region

PNS results may show some differences with respect to the full Navier-Stokes results. We also recall that numerical simulations are strongly affected by the numerical methodology, i.e., the accuracy, efficiency, physical and geometrical modeling, etc. The use of computational fluid dynamics then poses the question of how one can be sure of the accuracy of the computed solution, i.e., how reliable a solution is for the understanding of physical phenomena or for the estimation of critical issues." The problems associated with the computation of these unique flowfields are only exacerbated when there is a lack of experimental data available to help interpret the computational results.

Shereda et al.[8] discussed force, moment, and surface-pressure data that were obtained for PLES configurations at angles-of-attack from -4° to +20° at Mach numbers from 1.5 to 5.0. Three models were built and tested, having ellipticity ratios of 2.0:1, 2.5:1, and 3.0:1. All three models were 36.0 inches long. Based on limited comparisons, the parameters computed using the Supersonic/Hypersonic Arbitrary Body Program (S/HABP) did not agree well with the corresponding measured values. However, Shereda et al.[8] concluded: "During this study a number of different types of analysis codes have been used to generate theoretical results for data/theory comparisons. Both of the Euler codes used in this study, FLO57 and NSWC, did a very good job of predicting the pressure distribution, normal force and pitching moment at angles of attack of 6 degrees or less. Since the Euler codes are inviscid the axial forces predicted do not include the viscous effects and the correct prediction of the axial force coefficient requires that the viscous effects be accounted for."

Shepherd and Tod[9] discussed selected force, moment, and surface-pressure data from those that were reported by Shereda et al.[8]. Specifically, the data were for a PLES configuration having an ellipticity ratio of 2.5:1 at an angle-of-attack between 0° and 4° at Mach numbers of 2.0 and of 5.0. Shepherd and Tod[9] compared these data with flowfield computations that they had generated using a Multiblock Euler Flow Code. Agreement between computed and measured normal force coefficients was good at both Mach numbers for all angles-of-attack. However, Shepherd and Tod[9] concluded that the failure of the Euler Flow Code to model the boundary layer consistently led to under-prediction of the surface pressures, both on the windward and on the leeward surfaces.

Edwards and Roper[10] reported on a computational assessment of the static and of the dynamic coefficients for a PLES body at hypervelocity speeds, specifically, Mach 5 to Mach 9. Flow fields computed using CHASM, a parabolized Navier-Stokes (PNS) code, were compared with second-order shock-expansion (SOSE) and with Newtonian solutions that were generated using the DATCOM Code. The computational results were also compared against the experimental results that were obtained in the Cranfield University Gun Tunnel at Mach 8.2. The three computational methods not only correctly predicted the experimental trends, but were in generally good agreement with the experimental data. While the SOSE method proved best at predicting the drag coefficient, CHASM provided the better predictions for the lift coefficient, for the pitching-moment coefficient, and for the lift-to-drag ratio.

Surface-pressure measurement[11] and force-and-moment measurements[12] have been obtained in experimental programs that have been conducted in the Tri-Sonic Wind-Tunnel (TWT) at the Aerodynamic Research Center (ARC) at the U.S. Air Force Academy (USAFA). Flow visualization data were obtained in the form of schlieren photographs and surface oil-flow patterns that were obtained during these test programs. Data were obtained at a Mach number of 4.28 over a range of Reynolds numbers (based on the free-stream conditions and the model length) of 12.47×10^6 to 19.96×10^6 over an angle-of-attack range from -11° to +11°. The data from these wind-tunnel tests were compared with computations generated using the "$Cobalt_{60}$ code"[13], which was run on the Beowulf cluster at the High-Performance Computing Facility (HPCF) at the ARC. It should be noted that the experimental and the computational parts of this investigation were conducted concurrently in a double-blind fashion. That is, the results from the experimental effort were not used to influence the way in which the results from the CFD effort were produced and vice versa. The flow fields for slender (one-half) power-law elliptic section (PLES) configurations in a Mach 4.28 air-stream, as determined from the information generated through tests in the Tri-Sonic Wind Tunnel (TWT) and through the computations made using $Cobalt_{60}$ are discussed in the present report.

2. Research Shape

The "H3" configuration[10] studied in this effort is depicted in Figure 1. The H3 is a one-half power-law projectile with a 0.6 aspect elliptic cross-section. The cross-sectional variation of the body that is given by the one-half power law is

$$r = kx^{0.5} \tag{1}$$

where k is a constant for constant θ and the x-axis origin is at the nose of the projectile. The H3 length is given as 540 mm and the major base diameter is 60 mm[10]. Note that the length, major base diameter, and elliptic ratio (given as 0.6) are all that is required to define this shape.

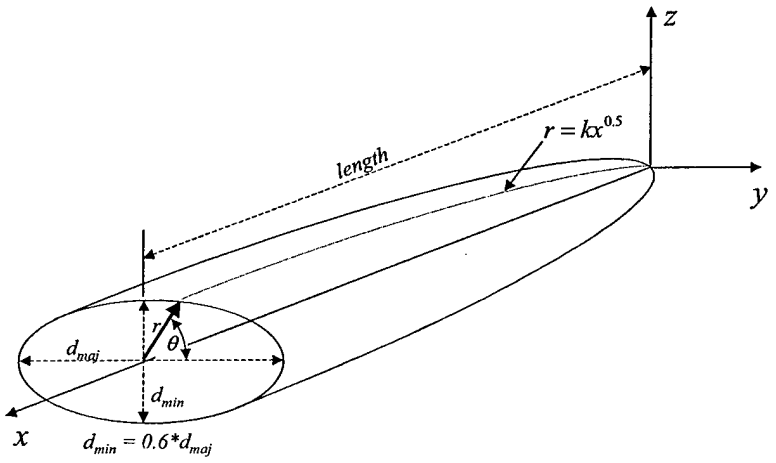

Figure 1. H3 model geometry

SECTION II

WIND TUNNEL TESTING

1. Wind Tunnel Test Facility

The experimental investigation utilized the Tri-Sonic Wind Tunnel (TWT) of the Aeronautical Research Center (ARC). The TWT is a blow-down facility that discharges to the atmosphere, as shown in Figure 2. For a run, the air passes from the holding tanks, through a series of control valves, into a stagnation (stilling) chamber, through a convergent/divergent nozzle, and into the test section, which is 1-foot by 1-foot square. The total pressure in the stagnation chamber (P_{t1}) is sensed by a transducer having a full-scale range of 300 psia with a combined nonlinearity and hysterises of ±0.3% full scale. The maximum total pressure in the stagnation chamber, which occurs at the higher Mach numbers (see Figure 3), is 250 psia. The total temperature in the stagnation chamber is sensed by a Type E (chromel/constantan) thermocouple capable of measuring -328°F to 1652°F with a sensitivity of 37.7±V/°F. The total temperature can be varied only slightly, being 560°R ±20°R.

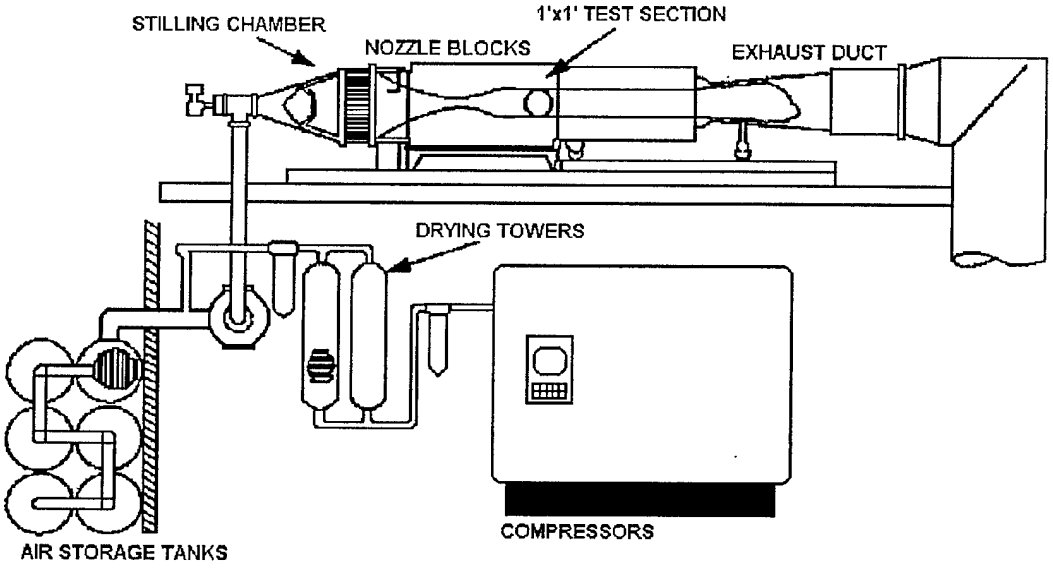

Figure 2. Schematic of USAF Academy Tri-Sonic Wind Tunnel

Fixed nozzle blocks form the convergent/divergent nozzle through which the air accelerates from the stagnation chamber into the test section. By selecting from the nozzle blocks that are available, one can provide test section Mach numbers at specific, selected design values in the range of 0.14 to 4.50. As shown in Figure 3, the operating

range of total pressure in the tunnel reservoir (P_{t1}) is a function of the test-section Mach number. By varying the pressure in the stagnation chamber of the TWT, one can control the unit free-stream Reynolds number in the test section. Depending upon the test-section Mach number, it is possible to generate free-stream unit Reynolds numbers from approximately 6×10^6 per foot to approximately 36×10^6 per foot.

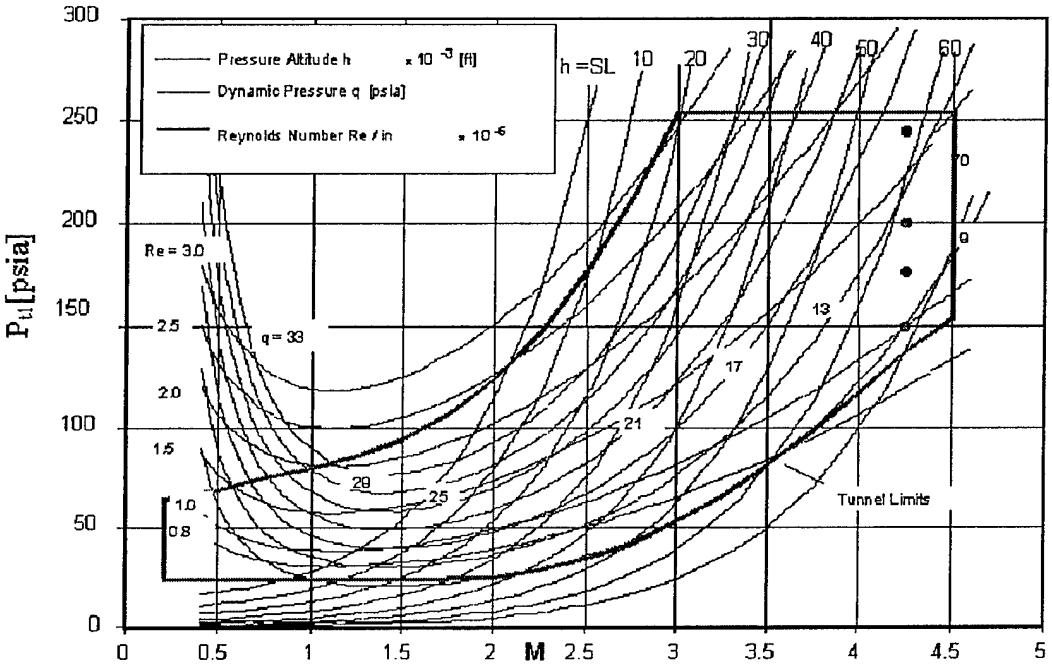

Figure 3. USAFA Tri-Sonic Wind Tunnel performance envelope

The run time is a function of the total temperature (T_{t1}), the total pressure in the tunnel reservoir (P_{t1}), and the nozzle throat area (which, since the cross-section area of the test section is fixed, relates uniquely to the Mach number in the test section). Usable run times range from 20 seconds to 420 seconds.

2. Test Conditions

For the nozzle blocks that were used in the present program, the free-stream Mach number in the test section was 4.28 ±0.04, which was determined from a facility calibration program. The total temperature was assumed to be constant at a value of T_{t1} = 560°R. Pressure measurements were obtained at stagnation pressures of approximately 150 psia, 175 psia, 200 psia, and 240 psia. Since the total temperature and the test-section Mach number are constants, the Reynolds number is directly proportional to the stagnation pressure. Thus, the corresponding Reynolds numbers, based on the free-stream conditions and on the model length are presented in Table 1.

Measurements of the forces, of the moments, and of the surface pressures were obtained at angles-of-attack of ±11°, ±10°, ±8°, ±6°, ±4°, ±2°, and 0° for all four Reynolds numbers.

Table 1. Correlation between the stagnation chamber pressure and the free-stream Reynolds number based on model length of 12.00 inches for the nominal test conditions of the present program

P_{t1} (psia)	$Re_L \times 10^{-6}$
150	11.74
175	13.69
200	15.65
240	18.79

3. Wind Tunnel Test Models

A computer-generated image of the baseline PLES configuration showing the coordinate system is presented in Figure 4. The origin of the coordinate system is at the apex of the model, with the x-axis corresponding to the longitudinal axis of the configuration. In accordance with the right-hand rule, the x-axis is positive to the left, when viewed from the rear of the model, and the z-axis is downward. The xy plane contains the major axis, while the xz plane contains the minor axis. The equations for the one-half power-law elliptic-section (PLES) configurations are

$$z = C_1 x^{0.5} \tag{2}$$

$$y = C_2 x^{0.5} \tag{3}$$

where the factors C_1 and C_2 define the thickness ratio of the model and the eccentricity of the elliptic cross section. For this report, the units for the physical coordinates (x, y, and z) in these two equations are inches. The lines traced out by these equations are connected by ellipses of eccentricity 5/3 centered on the x-axis. Thus,

$$C_2 = \left(\frac{5}{3}\right) C_1 \tag{4}$$

and

$$a = \left(\frac{5}{3}\right) b \tag{5}$$

The model geometries will be defined by a three-letter code. The first letter will be used to identify, whether the model was built at the Eglin Air Force Base (E) or at the U.S. Air Force Academy (A). The second letter will identify whether the model is a force-and-moment model (F) or a pressure model (P). The third letter will identify the thickness ratio of the model, which is defined by the magnitude of the parameters C_1 and C_2 (or a and b). For the baseline models, which are designated by the symbol B, C_1 =

0.119 and $C_2 = 0.198$. A pair of models (both a P and an F) were built at the U.S. Air Force Academy to study the effect of the thickness ratio on the comparison between the measured parameters with those from the computed flow fields. The modified models have a thickness ratio that is 4/3 that for the baseline models and are designated by the symbol M, $C_1 = 0.159$ and $C_2 = 0.264$.

Figure 4. Configuration geometry and coordinate system for slender, power-law elliptic-section model.

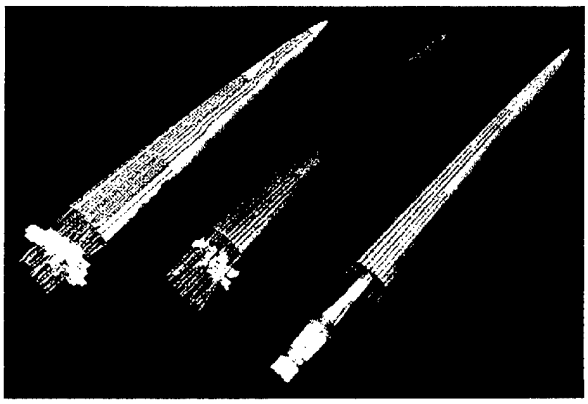

Figure 5. The models tested, from left to right: APM, APB, EPB

The reader should note that, for the models that were built at the Eglin Air Force Base, $L = 12.75$ *inches*. For the models that were built at the U. S. Air Force Academy, $L = 12.00$ *inches*. The Eglin model corresponds to the ``H3" configuration. The 12.00 inch baseline Academy model is the H3 model with the final 0.75 inches removed, in order to fit the entire model into the calibrated portion of the test section. For the pressure measurements these two models are equivalent, since all pressure measurements were taken well forward of 12.00 inches. For the force and moment measurements, the models are not equivalent. Presented in Figure 5 and in Table 2 is a summary of the nomenclature and of the dimensions of the models for which data relevant to the present report were obtained.

Table 2. The nomenclature and the dimensions of the models for which data relevant to the present report were obtained

	L (in.)	$a(=L_{ref})$ (in.)	b (in.)	S (in^2.)
EPB	12.75	1.417	0.850	0.946
APB	12.00	1.372	0.824	0.888
EFB*	12.75	1.417	0.850	0.946
AFB	12.00	1.372	0.824	0.888
APM	12.00	1.829	1.102	1.582
AFM	12.00	1.829	1.102	1.582

* Force-and-moment data for the EFB model were obtained in the DREV Tri Sonic Wind Tunnel[14]

For the EPB and for the APB models, twenty orifices, flush-mounted in the model's surface, were used to sense static pressures acting on the model during a run. Although the "E" and the "A" models were of different length L, the pressure orifices were located in one of two planes that were the same distance from the apex regardless of the length of the model, i.e., $x = 4.50$ *inches* and $x = 9.00$ *inches*. The locations of the pressure orifices are presented in Figure 6 and in Table 3. Eight orifices were located in a cross-section plane that was nominally 4.50 inches from the apex of the model. Twelve orifices were located in a cross-section plane that was nominally 9.00 inches from the model apex. In this report, spanwise pressure distributions at a station will be presented as a function of the dimensionless distance from the pitch plane, i.e., y/y_{max}, where y_{max} is the maximum value of y for that station. The orifices in the $x = 4.50$ *inches* plane are all meant to be located on the port side of the model, i.e., at positive values of y. Conversely, the orifices in the $x = 9.00$ *inches* plane are all meant to be located on the starboard side of the model, i.e., at negative values of y. This was done to simplify installing the hypodermic tubing in the model. However, model construction techniques resulted in the actual locations of the pressure orifices being slightly different than the specified locations. This can be seen in the pressure-orifice locations presented in Table 3 for the EPB model. Orifice no. 1, which was in the $x = 4.50$ *inches* plane, had a small negative y-coordinate.

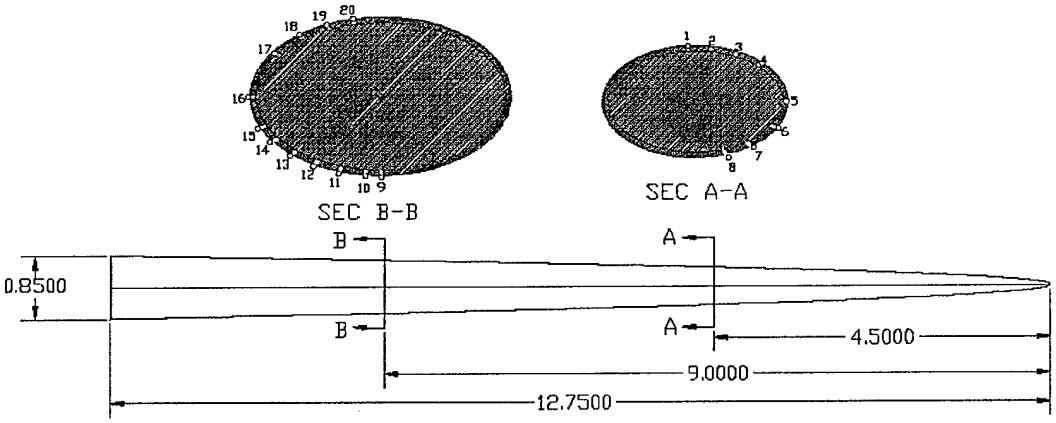

Figure 6. Location of the surface pressure ports for the APB and EPB models

A similar philosophy was used for locating the orifices to provide surface-pressure data for the APM model. However, because the APM model had a greater thickness ratio, it could accommodate 22 orifices, eleven at $x = 4.50$ *inches* and eleven more at $x = 9.00$ *inches*. The locations of the pressure orifices of the APM model are presented in Figure 7 and in Table 4.

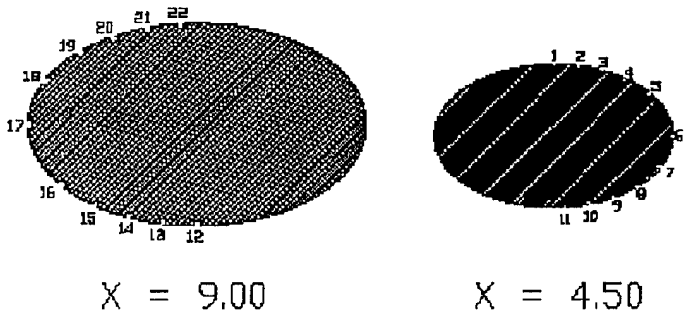

Figure 7. Location of the surface pressure ports for the APM model

Table 3. Locations of the static pressure orifices for the EPB and APB models.

Port	*x (in.)*	*x/L*	*y (in.)*	y/y_{max}	*z (in.)*	z/z_{max}
1	4.5	0.353	-0.033	-0.080	-0.249	-1.000
2	4.5	0.353	+0.072	+0.175	-0.234	-0.922
3	4.5	0.353	+0.184	+0.448	-0.210	-0.793
4	4.5	0.353	+0.284	+0.691	-0.161	-0.562
5	4.5	0.353	+0.411	+1.000	0.000	0.000
6	4.5	0.353	+0.376	+0.915	+0.121	+0.478
7	4.5	0.353	+0.263	+0.640	+0.207	+0.818
8	4.5	0.353	+0.150	+0.365	+0.253	+1.000
9	9.0	0.706	-0.130	-0.216	+0.364	1.000
10	9.0	0.706	-0.250	-0.415	+0.360	+0.989
11	9.0	0.706	-0.375	-0.622	+0.347	+0.953
12	9.0	0.706	-0.484	-0.803	+0.315	+0.865
13	9.0	0.706	-0.603	-1.000	+0.266	+0.731
14	9.0	0.706	-0.560	-0.929	+0.205	+0.563
15	9.0	0.706	-0.506	-0.839	+0.142	+0.390
16	9.0	0.706	-0.417	-0.692	0.000	0.000
17	9.0	0.706	-0.311	-0.516	-0.195	-0.562
18	9.0	0.706	-0.196	-0.325	-0.275	-0.793
19	9.0	0.706	-0.071	-0.118	-0.320	-0.922
20	9.0	0.706	0.000	0.000	-0.347	-1.000

Table 4. Locations of the static pressure orifices for APM model.

Port	*x (in.)*	*x/L*	*y (in.)*	y/y_{max}	*z (in.)*	z/z_{max}
1	4.5	0.353	0.000	0.0	-0.337	-1.000
2	4.5	0.353	0.112	0.2	-0.301	-0.894
3	4.5	0.353	0.224	0.4	-0.261	-0.775
4	4.5	0.353	0.336	0.6	-0.213	-0.632
5	4.5	0.353	0.448	0.8	-0.150	-0.447
6	4.5	0.353	0.560	1.0	0.000	0.000
7	4.5	0.353	0.504	0.9	0.106	0.316
8	4.5	0.353	0.392	0.7	0.184	0.548
9	4.5	0.353	0.280	0.5	0.238	0.707
10	4.5	0.353	0.168	0.3	0.281	0.837
11	4.5	0.353	0.056	0.1	0.319	0.949
12	9.0	0.706	0.000	0.0	0.476	1.000
13	9.0	0.706	-0.158	-0.2	0.426	0.894
14	9.0	0.706	-0.317	-0.4	0.369	0.775
15	9.0	0.706	-0.475	-0.6	0.301	0.632
16	9.0	0.706	-0.634	-0.8	0.213	0.447
17	9.0	0.706	-0.792	-1.0	0.000	0.000
18	9.0	0.706	-0.713	-0.9	-0.150	-0.316
19	9.0	0.706	-0.554	-0.7	-0.261	-0.548
20	9.0	0.706	-0.396	-0.5	-0.337	-0.707
21	9.0	0.706	-0.238	-0.3	-0.242	-0.837
22	9.0	0.706	-0.079	-0.1	-0.451	-0.949

Note that the pressure measurements from those orifices on the top of the vehicle, i.e., those having negative *z*-coordinates, are on the leeward surface when the model is at a positive angle-of-attack. Furthermore, the pressure measurements from those orifices on the bottom of the vehicle, i.e., those having positive *z*-coordinates, are on the leeward surface, when the model is at a negative angle-of-attack. Thus, one can combine the data from two stops on the alpha sweep (combining the pressure measurements from the orifices having a negative *z*-coordinate for a specific, positive alpha with the pressure

measurements from the orifices having a positive z-coordinate that were obtained at an alpha of the same magnitude, but negative in sign) to produce a composite, spanwise pressure distribution for the leeward surface. A similar approach would yield a detailed spanwise pressure distribution for the windward surface. This procedure requires that the symmetry of the model, the symmetry of the flow, and the run-to-run variations of the pressure measurements must be within acceptable limits. Data indicating that these three requirements were met will be presented in the section: "Results and Discussion."

For the models built at the U.S. Air Force Academy, the process was to build and test the "F" model first. Once the force-and-moment data had been obtained, the model was returned to the shop and the pressure tubing was placed in the model. Thus, the dimensions of the force-and-moment model were identical to those for the pressure model.

The measurements of the forces and of the moments were made using a six-component balance flush-mounted to the base of the model. The force coefficients (C_F), both for the axial force (X) and for the normal force (Z), were calculated using the relation that:

$$C_F = \frac{F}{q_1 S} \tag{6}$$

The coefficient for the pitching moment about the apex of the model, i.e., about $x = 0$, (C_{Mo}) was calculated using the relation that:

$$C_{M_o} = \frac{M_o}{q_1 S L_{ref}} \tag{7}$$

After mounting the model on the sting, two pressure probes were mounted on the sting. These probes were located on either side of the sting, approximately in-line with the yaw plane of the model and close to the base of the model. During the test runs, these probes sensed the static pressures in the base region. The two measurements were averaged to find the mean base pressure ($P_{b,ave}$), which was used in calculating the effective axial force (X_{eff}) and the effective axial-force coefficient ($C_{X,eff}$), as will be discussed later in the "Results and Discussion" section. When mounting the PLES models in the test section, great care was taken to ensure that the model was correctly aligned with the axis of the wind tunnel. However, small offsets ($\pm 0.2^{\circ}$) were unavoidable. Before the testing began and at regular intervals during each series of runs, the model offset angle was measured. The offset angle was then added to the sting angle to provide the actual angle-of-attack that was used in the analysis of the data.

THIS PAGE INTENTIONALLY LEFT BLANK

SECTION III

AEROBALLISTIC TESTING

1. Free Flight Facility

The tests were conducted in the US Air Force Aeroballistic Research Facility (ARF)[15]. This facility is operated and maintained by the Air Force Research Laboratory Munitions Directorate, Eglin AFB, FL. The ARF is an enclosed, instrumented, concrete structure used to examine the exterior ballistics of various free-flight projectiles. The 207-meter instrumented length of the range has a 16 m^2 cross section for the first 69 meters and a 25 m^2 cross section for the remaining length. The range has 131 locations available as instrumented stations of which 50 are currently used to house fully instrumented orthogonal shadowgraph stations. Besides the shadowgraph stations, the facility contains one laser-lighted photographic station located in the uprange end of the instrumented section. The range is an atmospheric test facility where the temperature and the relative humidity are controlled to 20 ±1 °C and less than 55%, respectively. A chronograph system provides the times for the projectile at each station. These times together with the spatial position and orientation obtained from the orthogonal photographs provide the basic trajectory data from which the aerodynamic coefficients are extracted.

2. Free Flight Model Design

Free-flight testing requires a statically stable model to determine the projectile's aerodynamic coefficients and stability derivatives.[16] A homogeneous H3 projectile would have its center of gravity at approximately 67% of the body length[10]. It was determined through initial predictions[10,24] that the center of pressure is at roughly 50-56% body length. It was then necessary to design a ballistic range model whose CG was ahead of the 50% body length position. Since there was some uncertainty about the exact location of the center of pressure for this configuration, a conservative desired location for the CG was selected at 47% body length.

Since the H3 configuration has more volume in the rear of the projectile, it was necessary to design a model with a heavy nose section and a lighter afterbody. The conventional means to adjust the center of gravity for a ballistic range model, as utilized in these test models, is to use a heavier material for the nose than for that of the base.

In order to get the center of gravity for the H3 configuration to 47%, a tungsten nose with an aluminum afterbody was required. Additionally, a hole was placed in the afterbody to further reduce its weight. The ballistic range model is depicted in Figure 8 and is a 25% scale version of the H3. Additionally, a sabot was required to house the model in the launch tube. The sabot is shown in Figure 9. The model's physical properties are given in Table 5.

Table 5. Free Flight Model Physical Properties

Reference Diameter (d_{maj}), mm	18.00
Reference Area ($A=\pi*(d_{maj}*d_{min})/4$), mm^2	152.68
Length (L), mm	162.0
Mass, g	70.6
I_x, g*cm2	9.34
I_y, g*cm2	1170.
X_{CG}, mm from nose	75.5

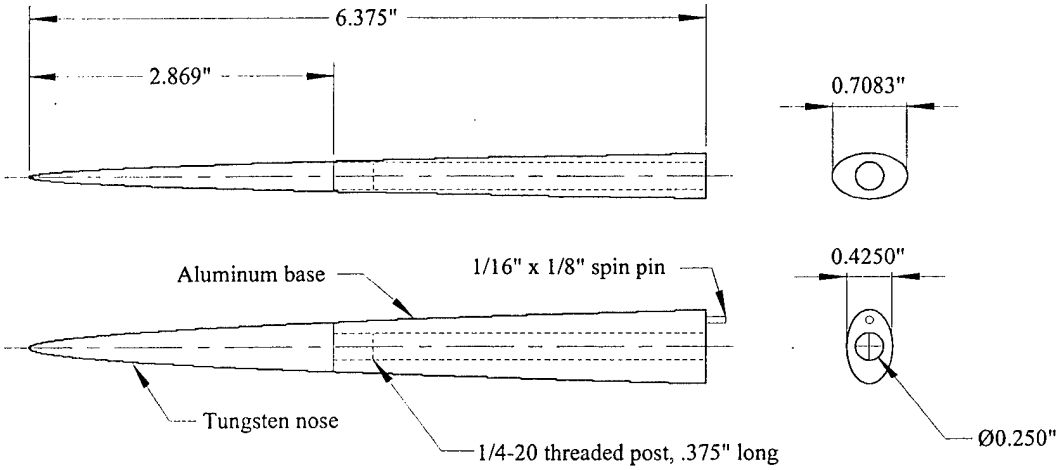

Figure 8. Free-flight ballistic range model

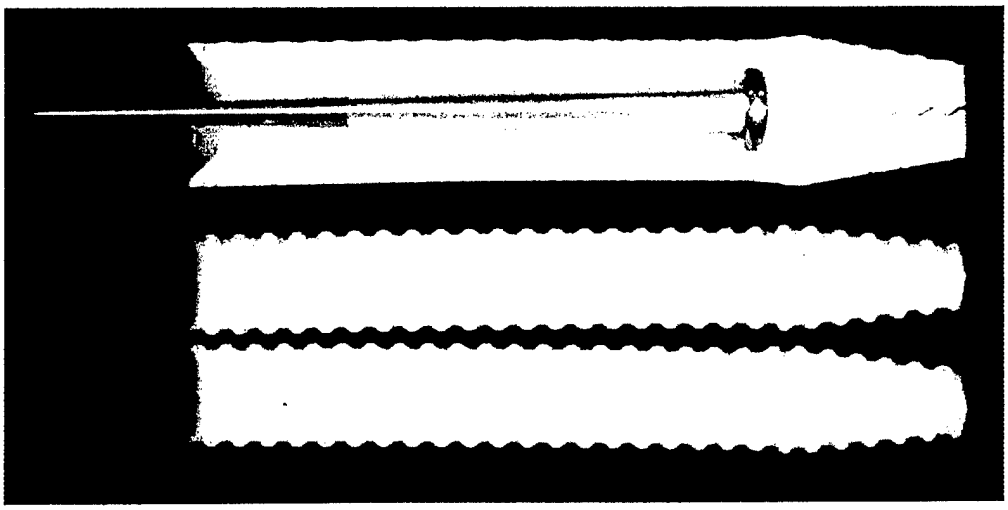

Figure 9. Free-flight model sabot

3. Free Flight Test Conditions

All test firings at the ARF were conducted at atmospheric pressure. As previously mentioned, the temperature and humidity within the ARF are controlled to about 21°C and 50%, respectively. The launch velocities ranged from Mach 3.0 to just below 5.0. Attempts to increase the launch velocity resulted in damage to the model. This damage was due to the launch acceleration causing "set-back" loads from the tungsten nose that buckled the aluminum afterbody. Aerodynamic Parameter Identification

From each set of free flight motion data the aerodynamic force and moment coefficients have been extracted. The essential steps of the data reduction are:

1. assemble the physical properties and atmospheric conditions,
2. read/analyze the film to determine the spatial position and orientation of the model,
3. mathematically model the test configuration's theoretical equation of motion, and
4. match these theoretical equations to the experimental data in order to determine the aerodynamic parameters of the model.

The complete process is described in Reference 17. The Comprehensive Automated Data Reduction and Analysis System (CADRA)[18] is used to read the film and calculate the trajectory. The trajectory matching process is accomplished using the Aeroballistic Research Facility Data Analysis System (ARFDAS)[17,19] and is depicted graphically in Figure 10.

ARFDAS incorporates a standard linear theory analysis[17,19,20] and a six-degree-of-freedom (6DOF) numerical integration technique[21]. The 6DOF integration routine incorporates the Maximum Likelihood Method (MLM) to match the theoretical trajectory to the experimentally measured trajectory.[19] The MLM is an iterative procedure that adjusts the aerodynamic coefficients to maximize a likelihood function. The use of this likelihood function eliminates the inherent assumption in least-squares theory that the magnitude of the measurement noise must be consistent between dynamic parameters (irrespective of units). In general, the aerodynamics can be nonlinear functions of the angle of attack, Mach number, and aerodynamic roll angle.

Each model fired in the ARF was initially analyzed separately, then combined in appropriate groups for simultaneous analysis using the multiple fit capability. This method provides a common set of aerodynamics that matches each of the separately measured position-attitude-time profiles. The multiple fit approach provides a more complete spectrum of angular and translational motion than would generally be available from any one trajectory considered separately. This increases the probability that the determined coefficients define the model's aerodynamics over the entire range of test conditions.

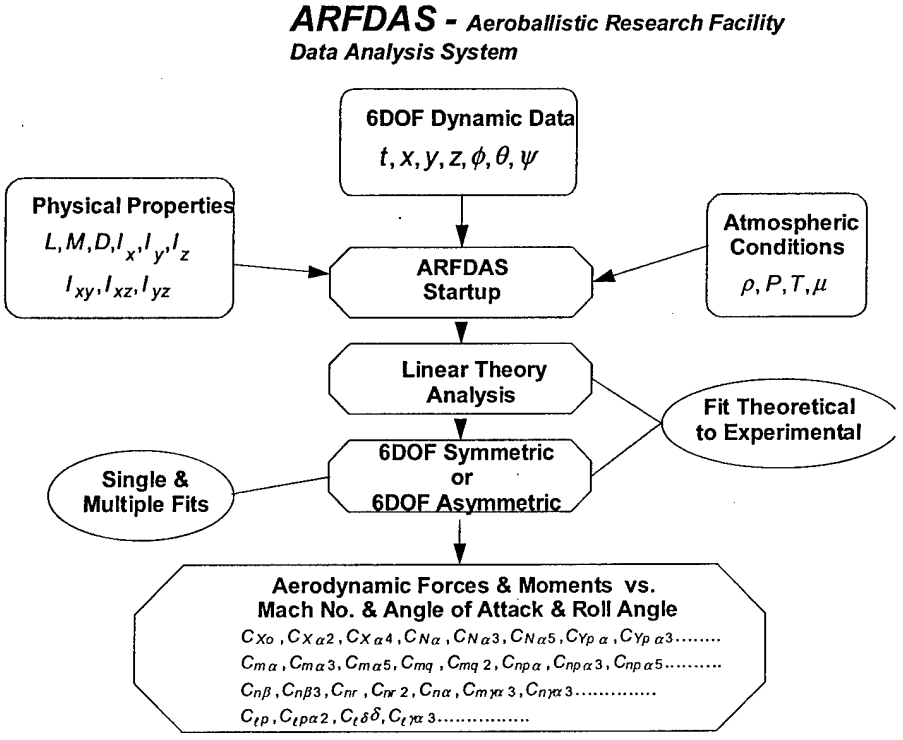

Figure 10. ARFDAS parameter identification process

4. Aerodynamic Predictions

Engineering level prediction capability for non-circular cross-section bodies is extremely limited. One of the only known codes for a variety of such configurations is the 1998 version of the US Naval Surface Weapons Center Aeroprediction Code (AP98)[22,23]. Predictions of the H3 configuration were performed[24] and will be presented in the results section of this report.

SECTION IV

COMPUTATIONAL ANALYSIS

1. Solutions of Wind Tunnel Data

Flow fields for the PLES configurations in a Mach 4.28 air-stream were computed using the December 1999 version of the $Cobalt_{60}$ code that had been developed by the Computational Sciences Branch at the United States Air Force Research Laboratory[13]. The aerodynamic parameters, thus computed, were compared with the corresponding experimentally determined aerodynamic parameters. $Cobalt_{60}$ is an implicit, parallel code that can be used to solve the full Navier Stokes equations, or simplifications thereof. The code can be set up to neglect the presence of a boundary layer adjacent to the surface, i.e., it can be set up to solve the Euler equations. In addition, the code can be set up, assuming that the boundary layer remains laminar over the entire surface of the configuration or that it transitions to turbulent flow at pre-defined locations on the surface. If transition is assumed to occur, the user of the code can select from a variety of turbulence models. The turbulence models available at the time these computations were made were: the one-equation turbulence model of Spalart and Allmaras[25] and the one-equation model of Baldwin and Barth[26]. Flow fields were computed for the three possible boundary-layer models: no boundary layer (using the Euler equations), a fully-laminar boundary layer, and a fully-turbulent boundary layer, so that no portion of the boundary layer is laminar. The Spalart-Allmaras turbulence model was used for those cases, where the boundary layer was assumed to be turbulent.

The unstructured grids that were used for the present study were generated using Gridgen, GRID-TOOL, and VGRIDns[27]. In order to minimize the computational resources required, the grid generation strategy took advantage of flow-field symmetry, where possible. One can take advantage of the fact that the zero angle-of-attack flow field is symmetric about both the pitch-plane and the yaw-plane. Thus, as shown in Figure 11, one needs to generate an unstructured grid for only one quadrant of the flow field. For the present study, approximately one million cells were used to compute the flow field, when the configuration is at zero angle-of-attack. For those cases where the angle-of-attack is not zero, but the yaw angle is, the grid-generation scheme took advantage of the fact that the flow was planar symmetric about the pitch-plane. Thus, the grid was mirrored about the yaw plane to provide a half-model of the flow field that contained approximately two million cells.

The inflow boundary conditions were taken to be those for the nominal test conditions for the runs that were conducted in the TWT. Flow-field solutions were computed for "all" angles-of-attack and for "all" configurations at $P_{tl} = 175\ psia$. Flow-field solutions were computed for selected configurations at $P_{tl} = 150\ psia$ and at $P_{tl} = 240\ psia$. These computations were made to investigate, if there were any Reynolds-number effects evident in the computed solutions.

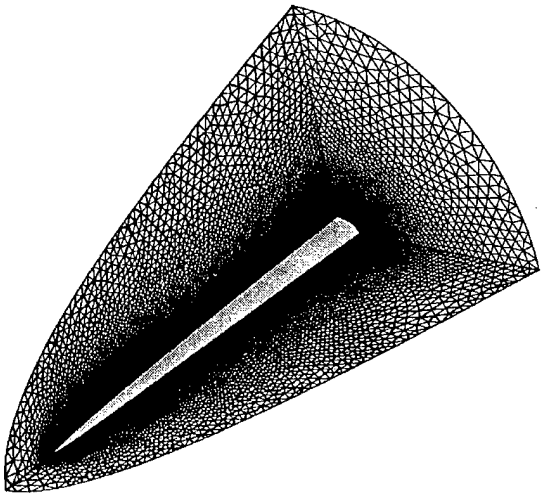

Figure 11. Cobalt$_{60}$ unstructured grid generated by VGRIDns for 0° angle of attack

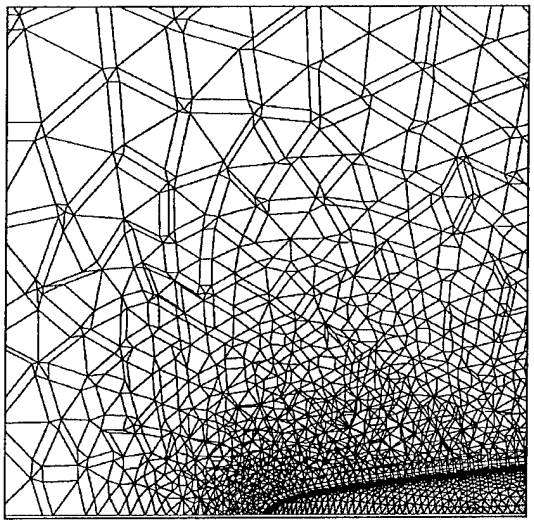

Figure 12. Detail of Cobalt$_{60}$ grid near the nose

The far-field boundaries were located far enough from the surface of the model so that the entire bow-shock wave could be captured over the entire angle-of-attack range, of interest to the present study (i.e., the entire shock layer could be computed for angles-of-attack from -11° to +11°). A close up of the unstructured grid in the vicinity of the model apex is presented in Figure 12. The area covered in Figure 12 corresponds to x in the range of *±0.5 inches*. As can be seen in Figure 11, the downstream boundary of the grid is co-planar with the base of the PLES configuration. Thus, the effect of base flow is not modeled in these calculations. When calculating the axial force acting on the model, it was assumed that pressure that acts over the base area of the model is equal to the free-stream static pressure.

2. Solutions of Free Flight Data

Flow fields for the H3 free flight configuration were computed using the June 2000 version of the Cobalt$_{60}$ code that had been developed by the Computational Sciences Branch at the U. S. Air Force Research Laboratory[13]. Cobalt$_{60}$ is an implicit, parallel code that can be used to solve the Navier-Stokes or Euler Equations. Reynolds-averaged turbulence models available in this version were: Spalart-Allmaras[25], Menter's Baseline[28], Menter's Shear Stress Transport[28], and Wilcox's 1998 k-ω[29] models. Forsythe et al.[30] tested these models on numerous benchmark cases, including a Mach 2.5 axisymmetric base flow. Menter's Baseline Model with compressibility correction was used for all the current calculations based on its performance in the base flow test case.

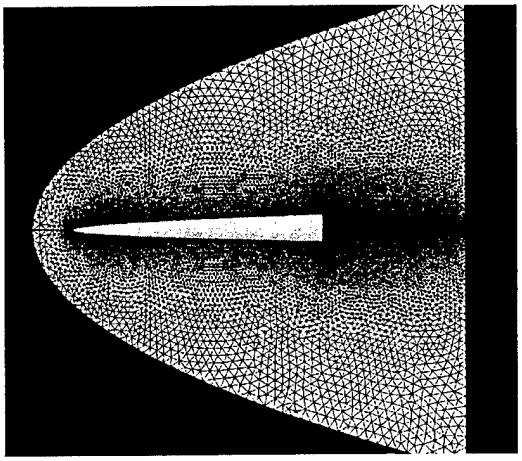

Figure 13. Computational domain for the alpha cases

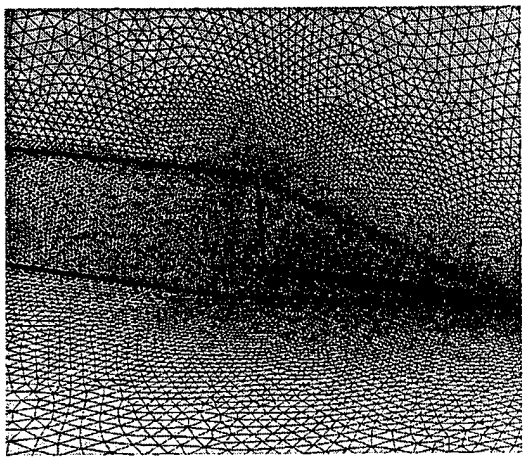

Figure 14. Grid close-up view of the base region for the zero degree cases

The unstructured grids that were used for the present study were generated using VGRIDns[31]. In order to minimize the computational resources required, the grid generation strategy took advantage of flow-field symmetry. For the zero degree case, only one quarter of the geometry was gridded. For the angle of attack cases, the grid was mirrored using the blacksmith utility[32] to provide a grid that modeled half of the geometry, as shown in Figure 13. This same process was applied for the beta cases. The quarter geometry grid contained 1.65 million cells while the half geometry grids contained 3.3 million cells. Prisms were used in the boundary layer, with an average first y^+ of 0.8 and a geometric stretching growth rate of 1.25. A close up of the base region is shown in Figure 14.

The far-field boundaries were located far enough from the surface of the model such that the entire bow-shock wave would be captured (~8.5 reference diameters). The upstream boundary was located approximately 1.4 reference diameters upstream of the nose. The downstream boundary was located far enough downstream from the base (~5.4 reference diameters) to recover to supersonic flow thereby preventing any reflections at the downstream boundary from affecting the solution upstream.

The inflow boundary conditions for the CFD simulations were taken to be representative of the ballistic range tests. A candidate flight condition was chosen at Mach 4.2 and comparable temperature and pressure values consistent with the ballistic range tests were specified. Figure 15 depicts the surface pressure contours, base flow streamlines, and calculated Schlieren flow structure for the 0° angle of attack case at Mach 4.2.

To calculate values of force and moment derivatives versus alpha and beta, solutions were generated at 0°, 1° alpha and 1° beta. The derivatives were then calculated

by comparing the forces and moments at 0° and 1°. By symmetry, all forces and moments except the axial force were zero for 0°.

Axial and normal forces, number of supersonic cells, and average first y^+ values were monitored during the runs to check for convergence. The run was considered converged when these values changed by less than 1% over 500 iterations in a row. This approach required approximately 4000 iterations. A grid refinement study was not conducted, however, previously sensitivity to grid resolution was explored for the forebody region only[33]. A coarser grid than the current one was seen to give grid independent solutions for the pressures at two axial locations. This is certainly not proof of a grid converged solution for the current study, especially in the base region.

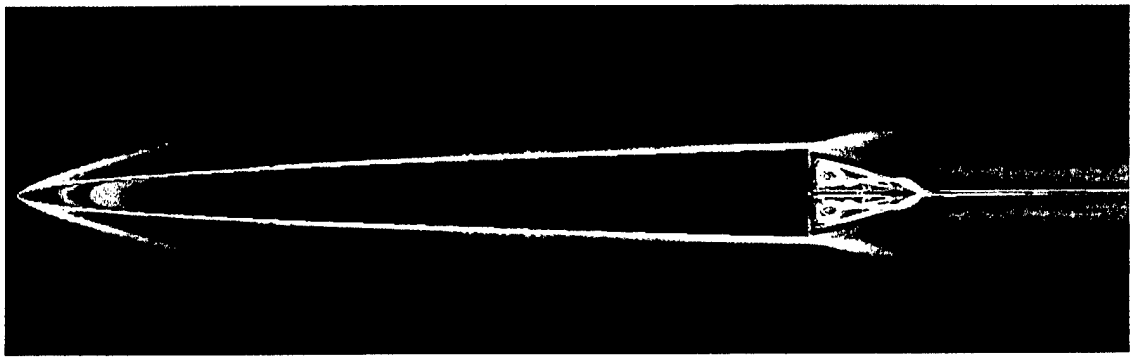

Figure 15. CFD results for zero alpha, Mach 4.2, free-flight conditions - surface colored by pressure, Schlieren on the symmetry plane, and streamlines in the base region

SECTION V

RESULTS AND DISCUSSION

1. Wind Tunnel Data

The comparison between the experimentally determined aerodynamic parameters and the corresponding computed values are presented in this report in four subsections. Surface-pressure measurements that were obtained at an angle-of-attack of 0°, ±6°, and ±10°/±11° and flow-visualization photographs will be presented in the first three subsections. The values of the experimentally determined parameters and of the computed parameters will be used to define the three different flow fields that occur over the range of alpha considered in the present report. When the angle-of-attack is zero, the flow field should be symmetric about both the *xy*-plane and the *xz*-plane. Six degrees angle-of-attack corresponds approximately to the upper limit for which the normal force coefficient is a linear function of the angle-of-attack. The third subsection will focus on the flow fields for the relatively high angles-of-attack, i.e., ±10°/±11°, where the flow field contains multiple vortices that result from flow separation. The force- and the moment-data will be discussed in the fourth and final subsection.

The Flow Field for 0° Angle-of-Attack

Surface streamlines that were observed in the oil-flow patterns obtained with the model at zero angle-of-attack and which are not presented in this report, were essentially parallel to the (vertical) pitch plane-of-symmetry. Thus, the oil-flow patterns indicated that there was some cross flow. As was noted in the Introduction, Kontis et al.[1] reported "the presence of a cross-flow from the high pressure sides at the ends of the major axis to the low pressure sides at the ends of the minor axis."

Cross flow also affected the shape of the bow shock wave. Mach-number contours that were computed using the $Cobalt_{60}$ code for a $Re_L = 14.55 \times 10^6$, which corresponds to a stagnation chamber pressure of *175 psia*, are presented in Figure 16 for the baseline configuration at cross sections of $x = 4.50$ *inches* and of $x = 9.00$ *inches*. The computed iso-Mach contours are approximately circular in cross section. The clustering of the iso-Mach contours corresponds to the location of the bow shock wave in the computed flow field. Schlieren photographs were obtained by Urena and Massett[34] while a power-law elliptic-section (PLES) model was rotated about its longitudinal, *x*-axis. Urena and Massett[34] also used a PLES model for which $z(x)$ and $y(x)$ vary as the one-half power-law, as given in equations (2) and (3), respectively. Since the model used in Reference 34 had a thickness ratio that was 1.60 times the thickness ratio of the baseline configuration, $C_1 = 0.190$ and $C_2 = 0.317$. Schlieren photographs were taken while varying the roll angle in thirty-degree increments. The trace of the bow shock wave in each Schlieren photograph was used to generate an experimental definition of the bow-shock-wave contours in the plane of $x = 4.50$ *inches* and in the plane of $x = 9.00$ *inches*.

The experimentally-determined cross sections thus determined for the bow shock wave are compared with the computed cross sections in Figure 17. The experimentally determined cross sections are in good agreement with the computed iso-Mach contours. Using Schlieren photographs, Kontis et al.[1] observed: "The distance between the shock wave and the body, for 0° incidence, is greater in the meridian plane containing the minor axis than in the meridian plane containing the major axis. The shock wave is not an ellipse similar to the body, but is "pushed in" toward the major axis and is "pulled out" from the minor axis." Thus, the results from the present investigation are consistent with the results reported by Kontis et al.[1].

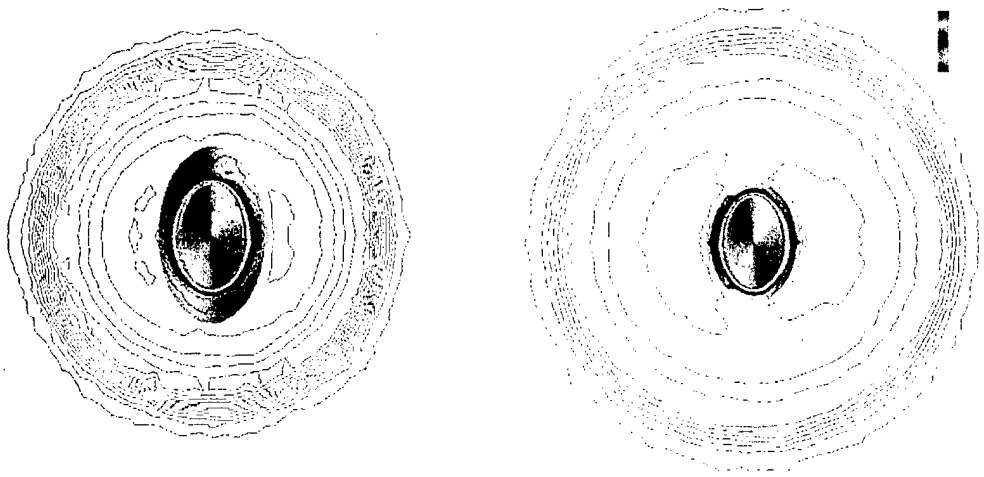

a) at $x=4.5$ *in.* b) at $x=9.0$ *in.*

Figure 16. Cobalt$_{60}$ calculated Mach contours

The trace of the bow shock wave in the vertical pitch plane ($y = 0$) is presented in Figure 18 for the baseline model at zero-angle-of-attack in a Mach 4.28 air-stream with $Re_L = 14.55 \times 10^6$. The Schlieren photograph is the top portion of the figure. The computed flow is below the plane-of-symmetry. The experimentally observed bow shock wave, as determined from the Schlieren photograph, is in good agreement with that from the Cobalt$_{60}$ computed flow-field solution. Note that the bow-shock-wave angle is curved near the apex of the model, but becomes a straight line (i.e., is linear) at points well downstream from the nose. Using the Schlieren photographs that were obtained as the large-thickness-ratio model was rotated in thirty-degree increments, Urena and Massett[34] measured the bow-shock-wave angle in the linear region. The experimentally-determined values for the bow-shock-wave angle, thus determined, and the corresponding computed values are presented as a function of the roll angle ϕ in Figure 19. The computed values and the experimentally determined values are in reasonable agreement.

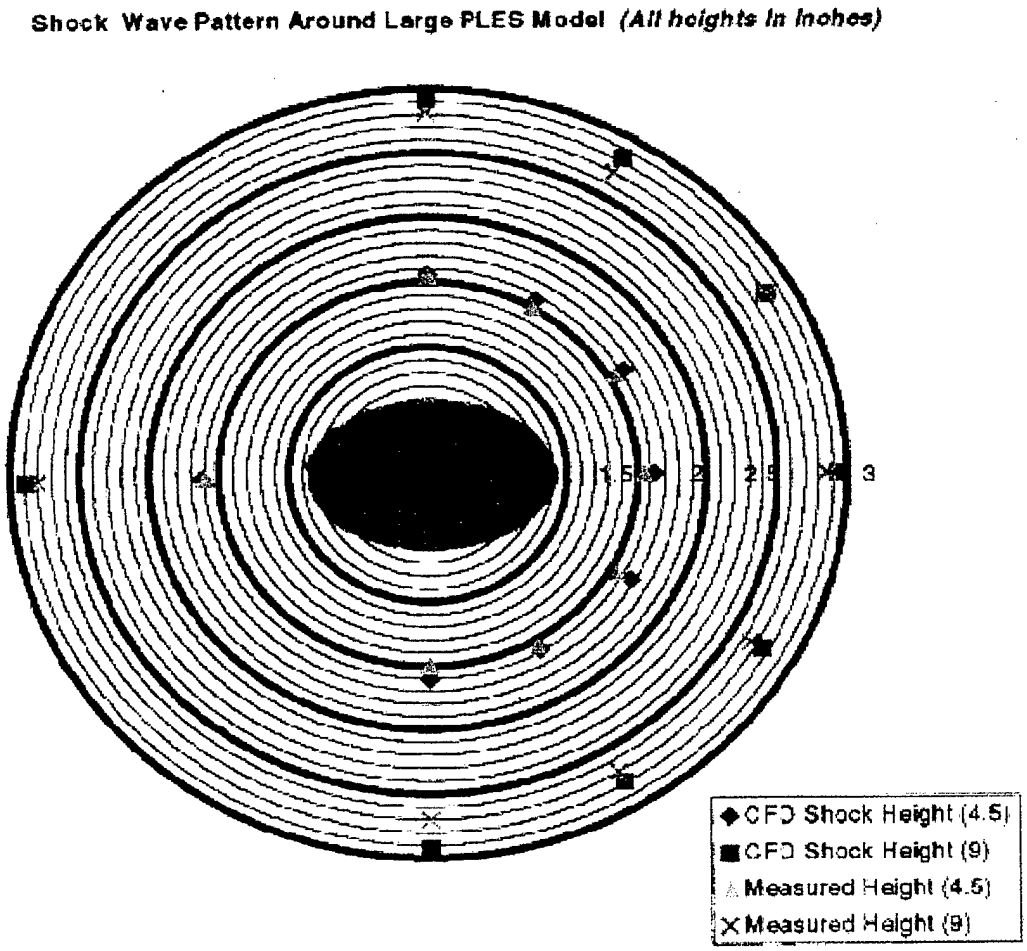

Figure 17. Cobalt$_{60}$ calculated Mach contours

Thus, it is seen that, for zero angle-of-attack, the cross section of the bow shock wave is almost circular both for station $x = 4.50$ *inches* and for station $x = 9.00$ *inches* for the baseline model (see Figure 16(a) and Figure 16(b)) and for the relatively large thickness-ratio model (see Figure 17). Furthermore, the slope of the bow shock wave in the linear region is almost independent of ϕ (see Figure 19). Thus, one would expect the static pressures on the surface of the model to be "approximately constant" at each of the two cross sections for which data were obtained.

Pressure measurements obtained at zero angle-of-attack and with the total pressure equal to *175 psia* are presented in Figure 20(a) for four different runs, two with the Eglin-built model (EPB) and two with the Academy-built model (APB). The typical test procedure was to obtain zero-angle-of-attack pressures twice during each run, once during the sweep through negative angles-of-attack and once during the sweep through positive angles-of-attack. The surface-pressure measurements from the upstream station, i.e., the station at $x = 4.50$ *inches*, are represented by the filled symbols. The surface-

pressure measurements from the downstream station, i.e., the station at $x = 9.00$ *inches*, are represented by the open symbols. As can be seen in the data of Figure 20(a), the experimental value for any test condition is ±3% of the arithmetic average of the four measurements for that orifice. Thus, the run-to-run variations, i.e., the repeatability of the measurements are well within the potential variations due to experimental uncertainty. It should be noted that there appears to be no significant, consistent bias for the measurements that come from the orifices located on the top surface of the model (i.e., negative values of z) relative to the measurements from the orifices from the lower surface of the model (i.e., positive values of z). The static pressures measured at orifices *17* and *18* (on the top of the model) are slightly greater than the measurements for orifices *13* and *14* (on the bottom of the model). Referring to Table 3 and to Figure 6 for the orifice locations, the reader can see these orifices are located at similar y/y_{max}. Conversely, the static pressures measured at orifice *20* (on the top of the model) are slightly less than the measurements for orifice *10* (on the bottom of the model).

Figure 18. The bow shock wave at $\alpha = 0^{o}$

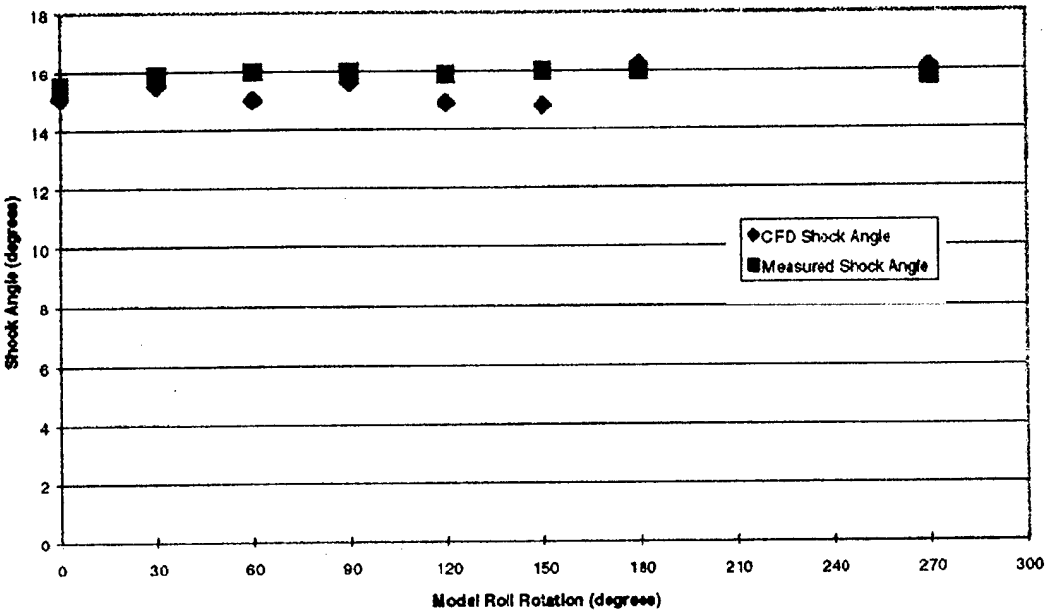

Figure 19. Bow shock wave angle measurements

The spanwise pressure distributions from four different runs are presented in Figure 20(b). However, unlike Figure 20(a), all four data sets are for the same model, i.e., the APB. The run-to-run variations in the pressure measurements obtained at zero angle-of-attack and with the total pressure equal to *175 psia* exhibit even smaller run-to-run variations than the measurements that were presented in Figure 20(a).

For all of the data presented in Figure 20, the pressure measurements from the station $x = 4.50$ *inches*, i.e., the filled symbols, are slightly greater than those from the station $x = 9.00$ *inches*, i.e., the open symbols. The slope of the baseline-model surface at these two x-stations is presented in Table 6, using equation (2) for the pitch-plane, and using equation (3) for the yaw-plane. The slope of the model surface decreases with x. Thus, if one uses a simple impact theory to estimate the local static pressure, one would expect that the pressure would decrease with x. However, as has been discussed, the cross flow that occurs even at zero angle-of-attack modifies the structure of the shock wave and, therefore, the static pressures acting on the model surface. Again, subtle complexities exist in the flow field for this relatively simple shape at zero angle-of-attack.

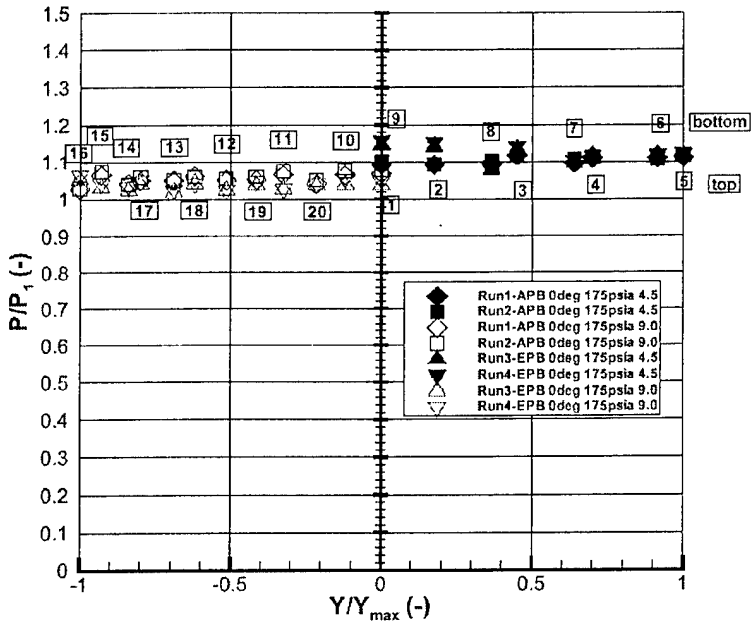

a) for the APB model and for the EPB model, with pressure taps labeled

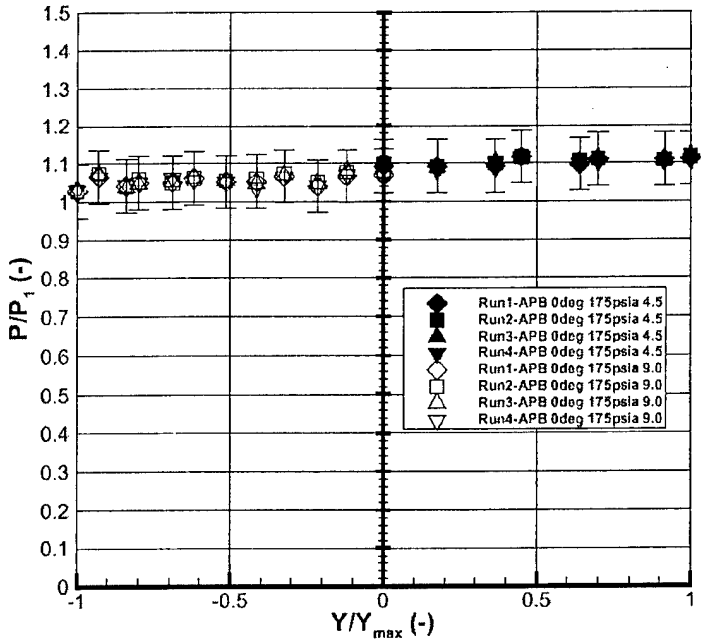

b) only for the APB model

Figure 20. Pressure measurements illustrating the repeatability of the data for $\alpha = 0$ and $P_{t1} = 175$ psia

Table 6. Slope of the baseline-model surface in the pitch plane (*dz/dx*) and in the yaw plane (*dy/dx*)

x-station (in.)	*dz/dx* (°)	*dy/dx* (°)
4.5	1.607	2.674
9.0	1.136	1.891

Pressure measurements obtained with the APB model at zero angle-of-attack are presented for all four Reynolds numbers in Figure 21. The pressure measurements are independent of the Reynolds number. Referring to Table 1, the reader will recall that, for the present tests, the Reynolds numbers based on the free-stream conditions and on the model length, ranged from 11.74×10^6 to 18.79×10^6. Although the authors do not have specific information about the boundary-layer transition criteria for this configuration, it is believed that the boundary layer would be turbulent over most of the model at each test condition. Thus, it is not surprising that the surface-pressure measurements do not depend on the Reynolds number for the range of conditions tested.

Included in Figure 21 are the spanwise pressure distributions computed using the $Cobalt_{60}$ code for a total pressure of *175 psia*. Flow field solutions were computed for three different models for the viscous boundary layer: (a) ignore the boundary layer altogether (i.e., solve the Euler equations), (b) assume that the boundary layer remains laminar over the entire length of the model, and (c) assume that the boundary layer is fully turbulent along the entire length of the model. There are no significant differences in the surface-pressure distributions computed for the three different models for the viscous boundary layer. Furthermore, the agreement between the computations and the measurements is considered very good.

The spanwise distributions of the static pressures for the APM configuration at zero angle-of-attack when the Reynolds number based on the free-stream condition and the model length is nominally 13.69×10^6 are presented in Figure 22. The experimentally determined values are in good agreement with the computed values. Recall that the thickness ratio of the APM model was 1.6 times the thickness ratio for the APB model. Thus, the thickness ratio does not appear to have a significant effect on the flow field, at least over the limited range of variation for the thickness ratio that was considered here.

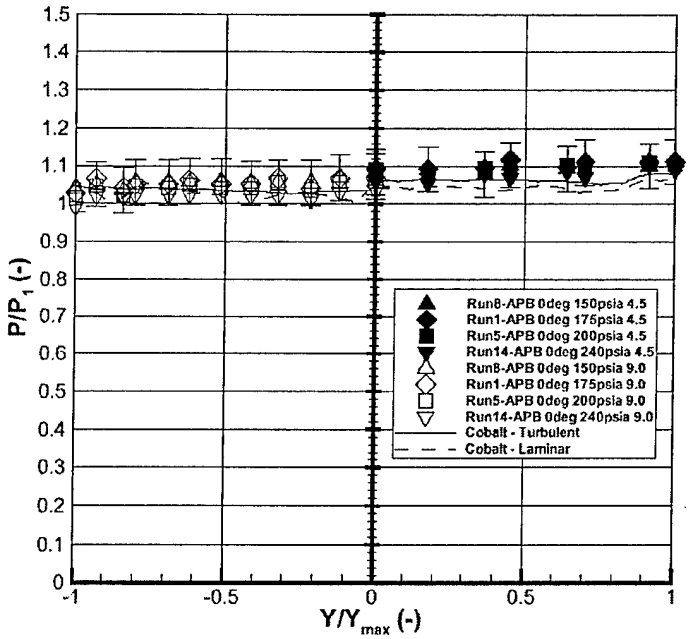

Figure 21.The effect of Reynolds number on the spanwise pressure distribution for $\alpha = 0^{o}$

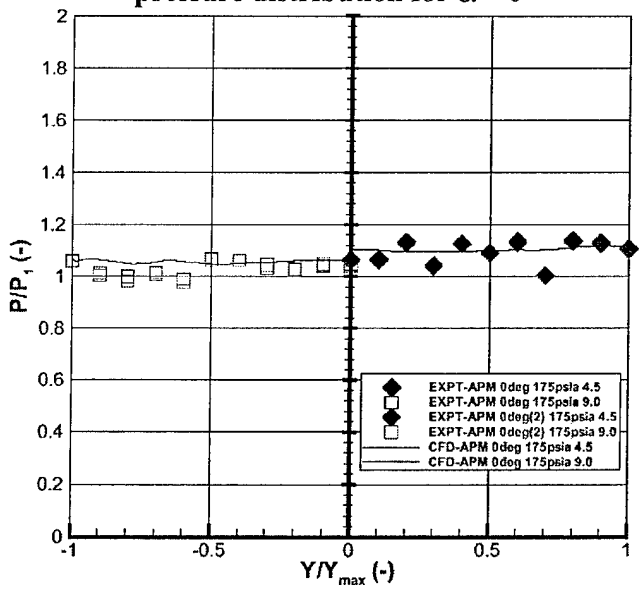

Figure 22. Comparison of pressures at 0^{o} for the APM model with CFD

The Flow Field for 6° Angle-of-Attack

Referring to Figure 23, the reader can see that cross-flow separation occurs at an angle-of-attack of 6°. The vector components of the velocity, as computed for planes of constant x (i.e., $x = 4.5$ *inches* and $x = 9.0$ *inches*), clearly indicate that the flow separates from the upper surface of the elliptic cross section in the vicinity of $y/y_{max} = 0.8$. Later in this section, we will see that an angle-of-attack of six degrees is slightly above the alpha range for which the normal force coefficient is a linear function of the angle-of-attack.

Experimentally determined spanwise pressure distributions for the APB and for the EPB model are compared in Figure 24 with the computations. The spanwise pressure distributions for the APM model are compared with the computations in Figure 25. These results are presented for a Reynolds number based on the free-stream conditions and the model length that is nominally 13.69×10^6. The measurements from the station $x = 4.50$ *inches* exhibit some scatter. In actuality, the three measurements from the region $0.15y_{max} \leq y \geq 0.70y_{max}$ that are greater than the computed values all were sensed at orifices located on the top of the models (i.e., having negative values of z). Conversely, the two pressure measurements from the region $0.15y_{max} \leq y \geq 0.70y_{max}$ that are very close in magnitude to the computed values are from the bottom of the models (i.e., having positive values of z). Since this is true both for the Academy-built model (APB) and for the Eglin-built model (EPB), the difference is attributed to a flow field phenomena rather than a model-construction difference. Furthermore, measurements of the model offset (i.e., the actual angle-of-attack of the model before or after a run when it should be zero) were taken on a regular basis. The model offsets were small, usually less than 0.2°, which was close to the uncertainty in our measurement. The differences between the pressures sensed at orifices on the top of the model and those from the bottom of the model far exceed what one would expect due to an error in the offset angle. Thus, the differences are attributed to weak waves crossing the tunnel, which could be seen in the Schlieren photographs. The waves, which can be seen in Figure 26, are attributed to small disturbances associated with the curvature of the nozzle wall, when the nozzle blocks were machined.

A horizontal line can be seen in the Schlieren photographs originating near the middle of the leeside of the model. The horizontal trace can be seen both for the positive angle-of-attack (Figure 26(a)) and for the negative angle-of-attack (Figure 26(b)). It is believed that this trace marks the boundary of the coalescence of the recirculating viscous cross flow in the leeward plane-of-symmetry. There is no indication of significant density gradients in the Schlieren photograph in the leeward flow upstream of the origin of this horizontal line. Thus, it is believed that, in the leeward flow near the nose, significant density gradients occur only in a thin, turbulent boundary layer.

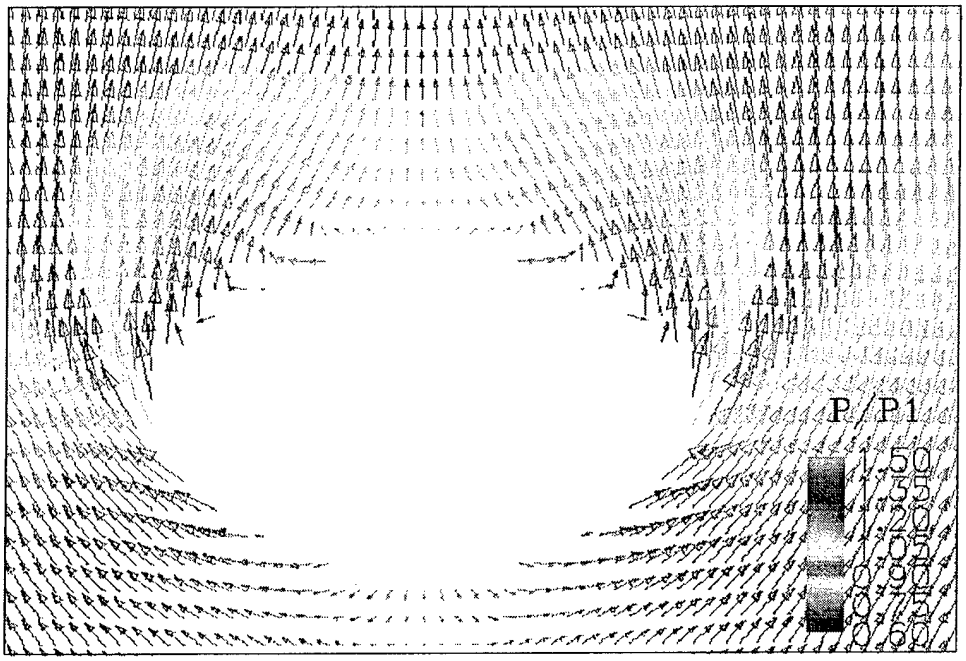

a) *x=4.5 in.*

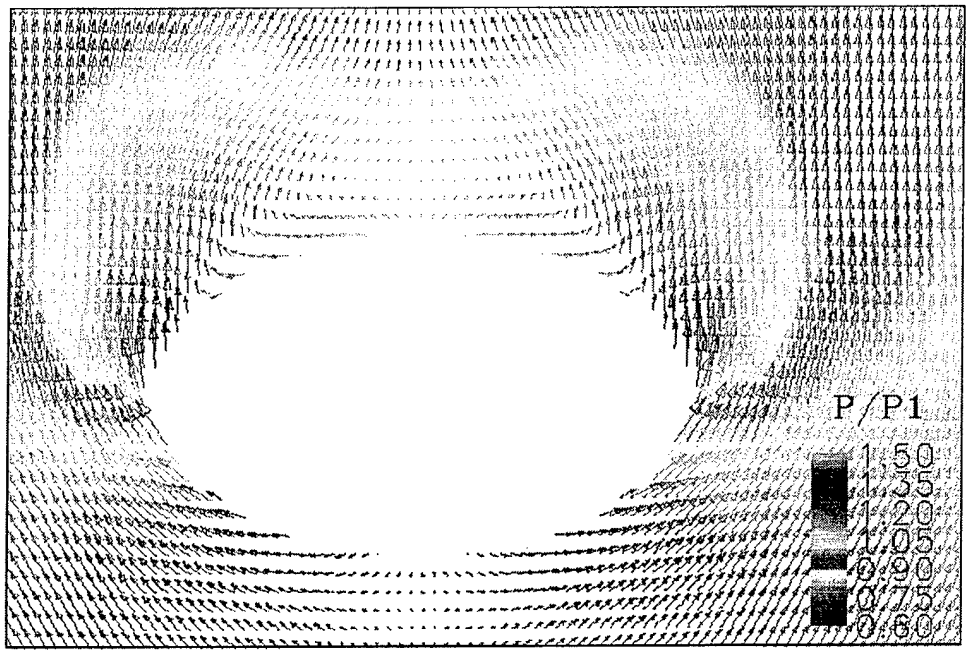

b) *x=9.0 in.*

Figure 23. Vector components of the velocity in planes of constant x (cross-section planes)

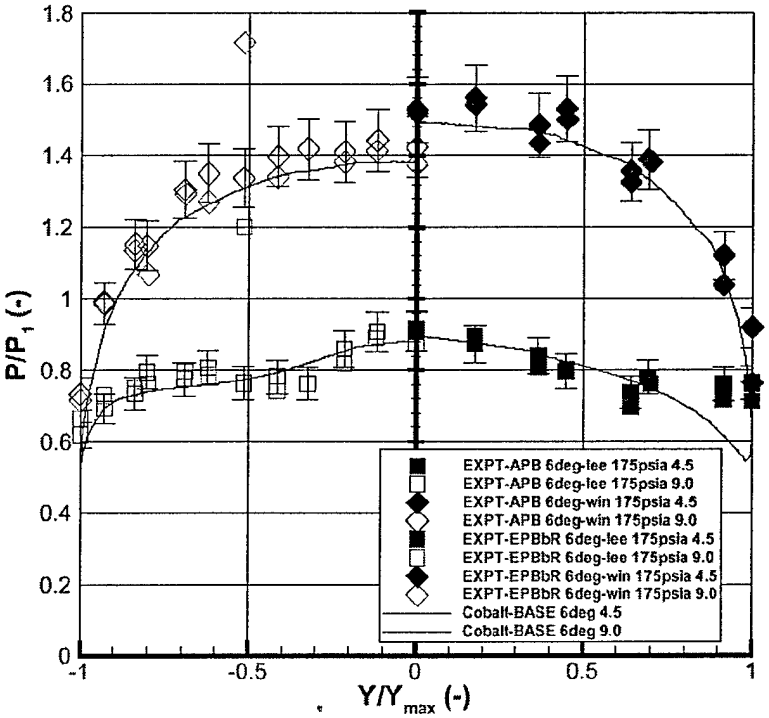

Figure 24. Surface pressures for the APB and EPB models at $\alpha = 6^{o}$

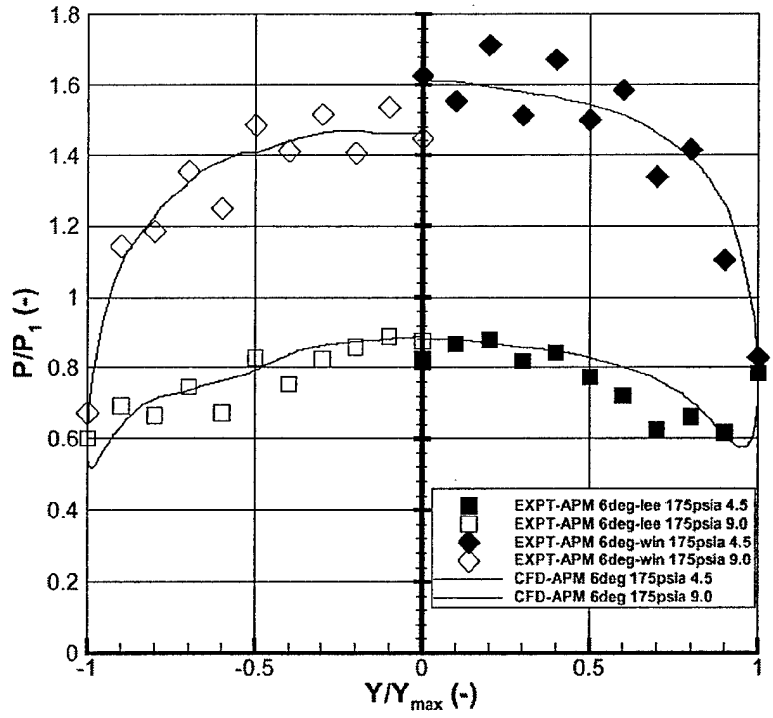

Figure 25. Surface pressures for the APM model at $\alpha = 6^{o}$

a) $\alpha = -6^o$

b) $\alpha = +6^o$

Figure 26. Schlieren photographs for the flowfield for the baseline configuration at an angle of attack of ± 6^o, P_{t1} = 175 psia

The Flow Fields for ±10°/±11° Angle-of-Attack

When the PLES configuration is inclined to the free-stream such that the angle-of-attack is in the range ±10°/±11°, the computations, oil-flow patterns on the surface of the model, and Schlieren photographs all indicate the existence of a free-shear-layer separation. This free-shear-layer separation creates helical vortices as the air particles in the free-shear-layer move both toward the leeward plane-of-symmetry and down the length of the model.

Presented in Figure 27 are static pressures on the surface of the model, iso-bar contours from the pitch plane of the flow field, and streamlines that have been taken from the flow-field solution that was computed using the $Cobalt_{60}$ code for the EFB model at an angle-of-attack of 11°. The computational model assumes a fully turbulent boundary layer for the entire length of the model. The computed flow field indicates the presence of two supersonic helical vortices, which coalesce in the leeward plane-of-symmetry. This is consistent with a free-vortex type of separation[2].

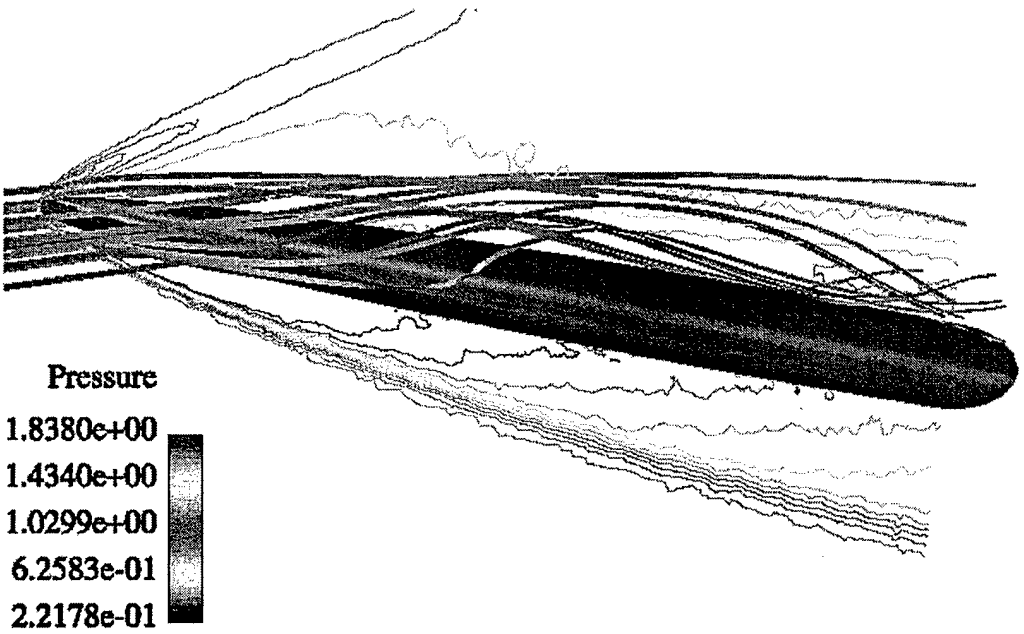

Figure 27. $Cobalt_{60}$ results at $\alpha = 11°$

However, oil-flow patterns that were observed on the surface of the EFB model when the model was at an angle-of-attack of 10° indicate a more complex flow field than was evident in the computed solution. Presented in Figure 28 are a side view and a leeward view of the oil-flow patterns obtained with the EFB model at an alpha of 10°. Note that the oil-flow patterns indicate the existence both of a primary- and of a secondary-separation location. The oil-flow pattern that appears in the side view of Figure 28(a) indicates that a flow separation occurred very near the yaw plane as the flow proceeded from the windward surface around the rapid change in cross-section slope for

large values of y. This is the primary separation location. The primary separation locations for several values of x are designated by the red symbols in Figure 29. Near the nose of the model, the oil-flow patterns indicate that the primary separation location is on the leeward surface. Further downstream, away from the nose of the model, the primary separation of the flow from the model surface takes place in the yaw plane, i.e., at the end of the major axis. Shereda et al.[8] presented similar findings for the primary separation locations from their tests.

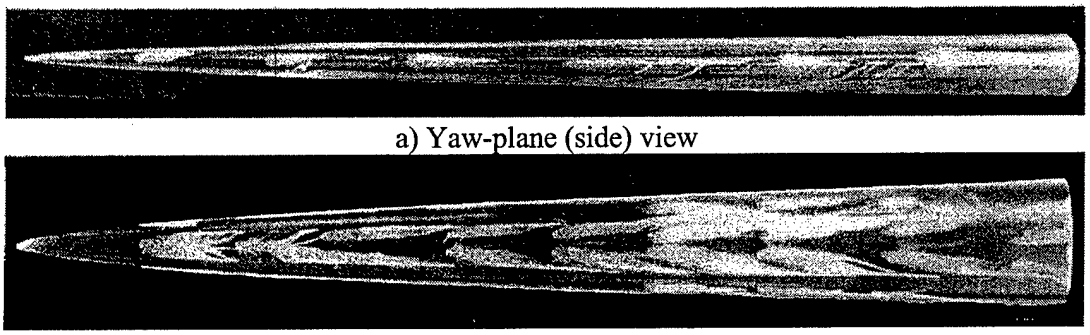

a) Yaw-plane (side) view

b) Leeward view

Figure 28. Oil flow patterns at $\alpha = 10^{o}$

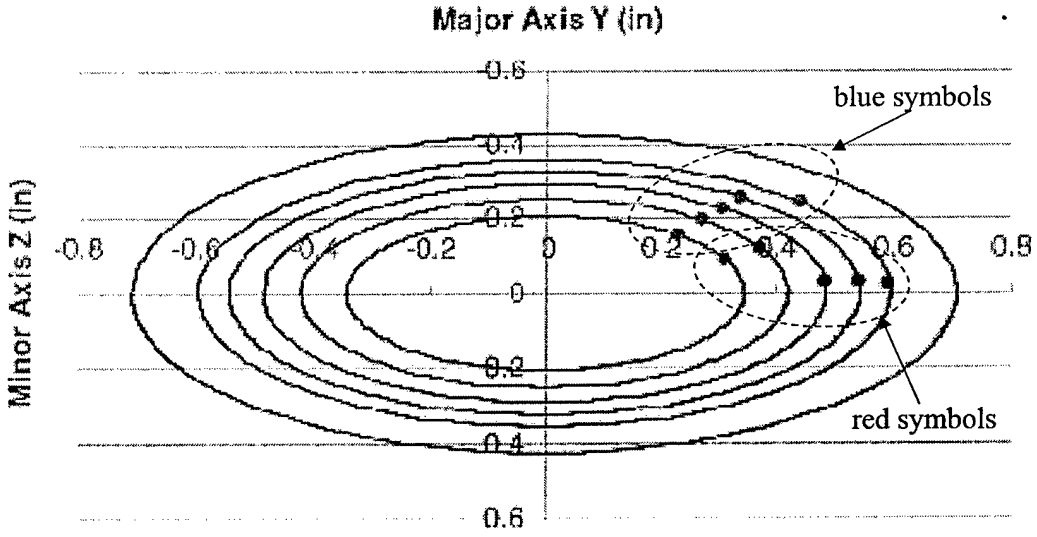

Figure 29. Primary and secondary separation locations at $\alpha = 11^{o}$

The free-shear-layer separation created a pair of helical vortices as the air particles in the free-shear-layer moved both toward the leeward plane of symmetry and down the length of the model. The two helical vortices are features both of the computed flow (refer to Figure 27) and of the experimentally observed flow field. The two recirculating,

helical vortices coalesced in the leeward plane-of-symmetry and then impinged on the surface. The trace marked "Feature of Interest" in the Schlieren photograph of Figure 30(a) marks the experimentally observed outer limit of the coalescing vortices. The trace "Feature of Interest" in Figure 30(b) marks the locally high densities in the leeward plane-of-symmetry taken from the "Schlieren option" for the computed flow field. It is believed that this trace in the computed flow field that is presented in Figure 30(b) also corresponds to the location of the outer limit of the vortex pair coalescing in the leeward plane-of-symmetry. Information to support this assumption is presented in Figure 31. In Figure 31 selected streamlines have been added to the computed density contours that were presented in Figure 30(b). Note that the maximum value of the negative z-coordinate for the helical vortices corresponds to the location of the "Feature of Interest" in the leeward plane-of-symmetry. Grids have been placed in Figure 30(a) and Figure 30(b) at the two x-stations where the static pressure ports are located. The experimentally determined locations of this trace (as taken from the Schlieren photograph) are in reasonable agreement with the computed locations (as determined from the density-gradient contours).

As the two recirculating, helical vortices coalesced in the leeward plane-of-symmetry and then impinged on the surface, they created an attachment line in the leeward plane-of-symmetry. The reattaching flow causes the pressures to be highest near the leeward plane-of-symmetry. See the spanwise pressure distribution presented in Figure 32. On the leeward surface of the model, the recirculating flow proceeded both downstream and away from the plane-of-symmetry. As shown in Figure 28(b), this flow produced a feather pattern in an oil film placed on the leeward surface. The oil-flow pattern is consistent with the pressure field. The spanwise component of the flow moved from the relatively high pressures near the leeward plane-of-symmetry. The pressure reached a minimum near the mid-span of the model, at $y \sim 0.5y_{max}$. As the spanwise component of the flow near the surface moved further from the plane of symmetry, it encountered an adverse pressure gradient. Refer to Figure 32. The oil-flow patterns of Figure 28(b) indicate that a second, imbedded free-vortex-type separation occurred long before the recirculating flow reached the yaw plane. As can be seen in Figure 28(b), oil accumulated along a line approximately *2/3* of the way to the edge of the model in the yaw plane. Because the oil continued to flow downstream, it is believed to be the demarcation line of an imbedded free-vortex-type of separation for the recirculating flow, the secondary separation. Thus, even for a relatively low angle-of-attack (i.e., 10°), the flow field around the power-law elliptical-section configuration contains both primary and secondary separation streamlines. The locations of the secondary separation location are indicated by the blue symbol in Figure 29. Oil-flow patterns presented by Shereda et al.[8] also exhibited secondary flow separation from the leeward surface.

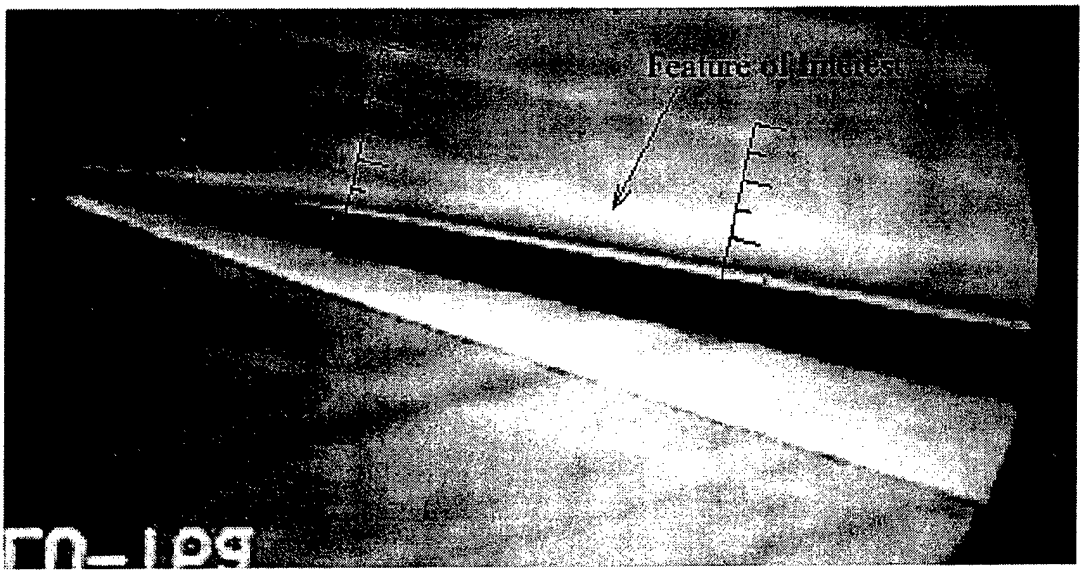

a) Experimental

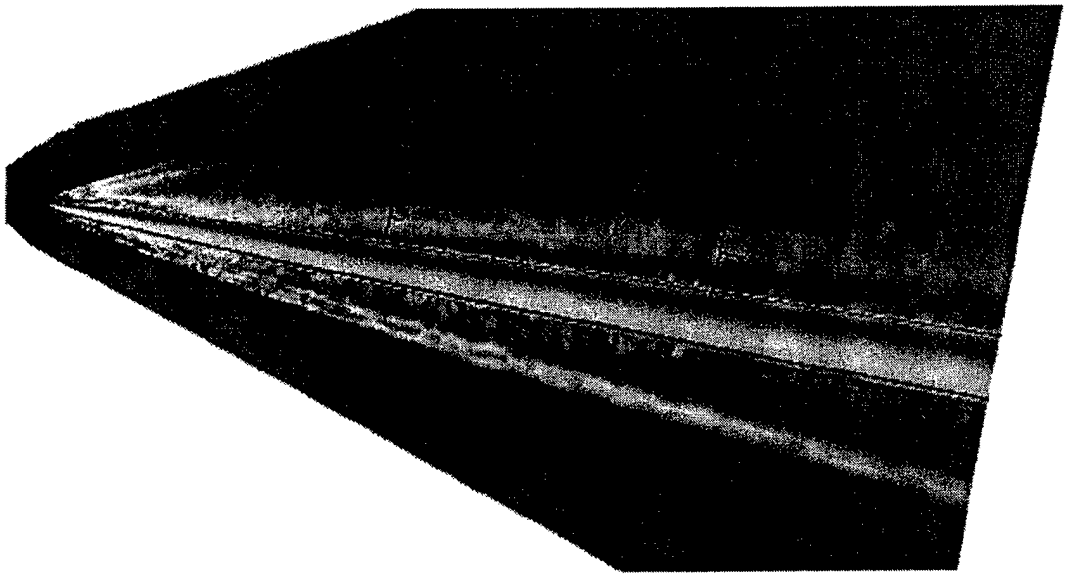

B) CFD (Cobalt$_{60}$ Computations)

Figure 30. Experimental and computational Schlieren images at $\alpha = 11^{o}$

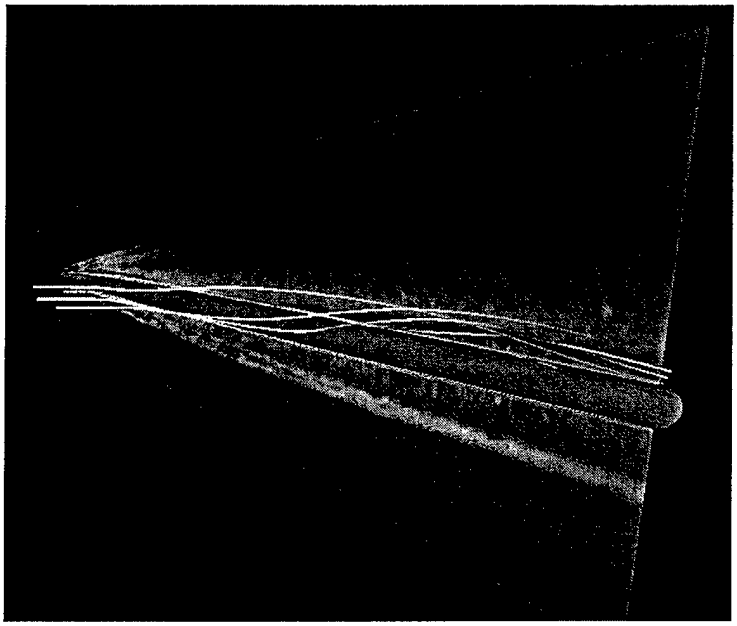

Figure 31. Computational flowfield using Schlieren option for $\alpha = 11^{o}$ with streamlines added

Fi

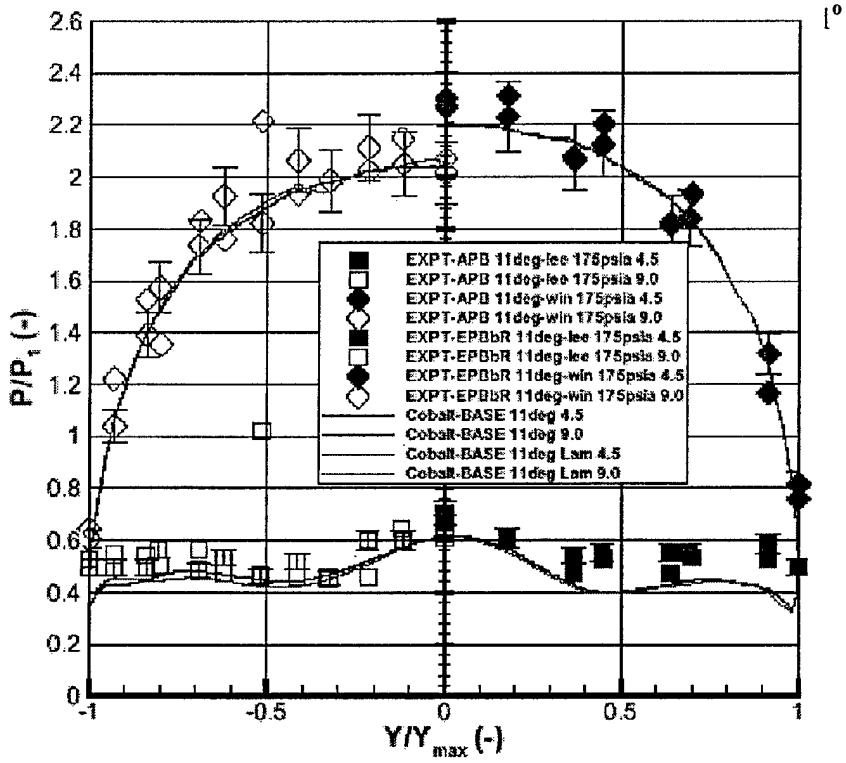

The experimentally determined spanwise pressure distributions for the APB and the EPB models at angles-of-attack of ±11° are presented in Figure 32. Consider the experimentally determined pressures for $x = 9.00$ *inches*, for which y is negative. The measurements from the top of Station *9.00 inches* are on the leeward surface, when the model is at an angle-of-attack of 11° (as represented by the filled diamonds). Similarly, the measurements from the bottom of Station *9.00 inches* are on the leeward surface, when the model is at an angle-of-attack of -11° (as represented by the open squares). Note that, although these measurements are from two different stops on the alpha-sweep, a single smooth curve through the two sets of data would represent the experimentally determined spanwise pressure distribution for the leeward surface. However, there are slight differences for the two sets of pressure measurements for the windward surface at Station *9.00 inches*. Although the differences were well within the experimental uncertainty, the measured values for the bottom surface at Station *9.00* (as represented by the filled squares) were slightly greater than the measured values from the top surface of Station *9.00*, when the model is at -11° angle-of-attack (as represented by the open diamonds). Refer to the Schlieren photographs presented in Figure 33(a) and Figure 33(b). A weak right-running wave can be seen impinging on the windward surface of the model, when the model is at +11° angle-of-attack. The wave impinges on the model at Station *9.00*, which corresponds to the location of the relatively high pressure measurements. The viscous/inviscid interaction associated with the weak impinging wave would explain the slight increase in these pressure measurements.

Force and Moment Data

The normal force coefficients for the baseline model built at the USAFA as measured at positive angles-of-attack are presented in Figure 34 for all four Reynolds numbers. The measured values for the normal force coefficient are independent of the Reynolds number over the range for which data were obtained. Included for comparison are the normal force coefficients computed using the Cobalt_{60} code. CFD solutions were obtained under the assumption that the boundary layer was fully laminar or that it was fully turbulent, using the turbulence model of Spalart and Allmaras[25]. For angles-of-attack of four degrees, or less, the lift coefficient is a linear function of the angle of attack, with the experimental values being slightly greater than computed values at a given angle-of-attack. For the angle-of-attack range where the normal force coefficient is a linear function of the angle-of-attack, the computational solutions indicate $C_{Z\alpha}$ is *0.0722* per degree whether the boundary layer is assumed to be fully laminar or fully turbulent. The corresponding value of $C_{Z\alpha}$ based on the experimental measurements is approximately *0.080* per degree. For the range of alpha, where the $C_{Z\alpha}$ is not constant, the differences between the experimentally determined normal force coefficients and those computed assuming that the boundary layer is fully turbulent, although small, increase with alpha. Although the boundary layer is believed to be turbulent at the high Reynolds numbers associated with this study, the normal force coefficients computed assuming the boundary layer is wholly laminar are in relatively good agreement with the experimental values at 11°.

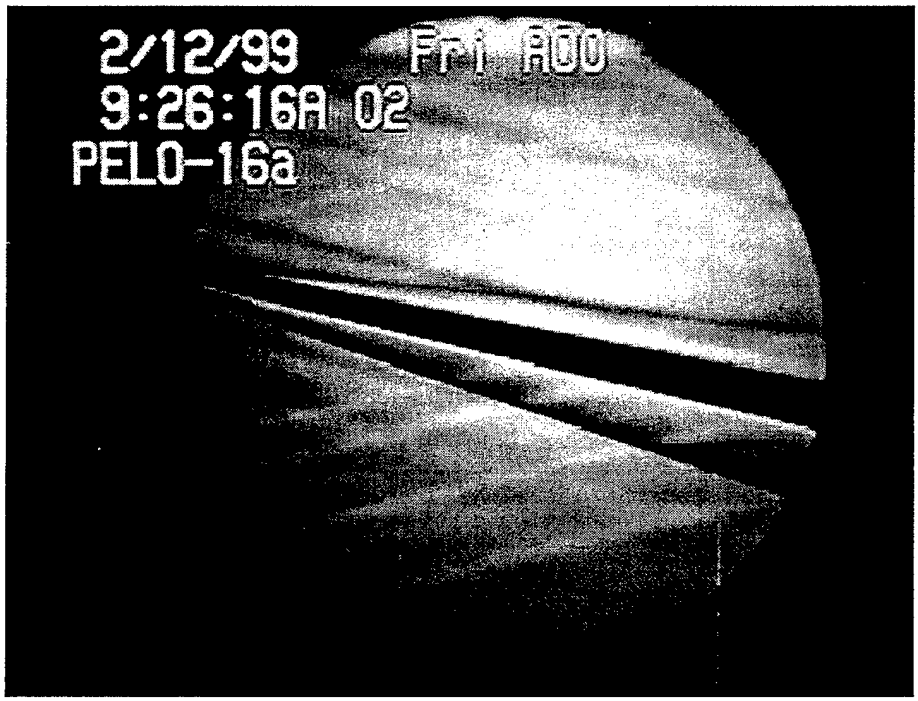

b) $\alpha = +11^{o}$

Figure 33. Schlieren photographs for the flowfield for the baseline configuration at an angle of attack of ± *11°*, P_{t1} = *175 psia*

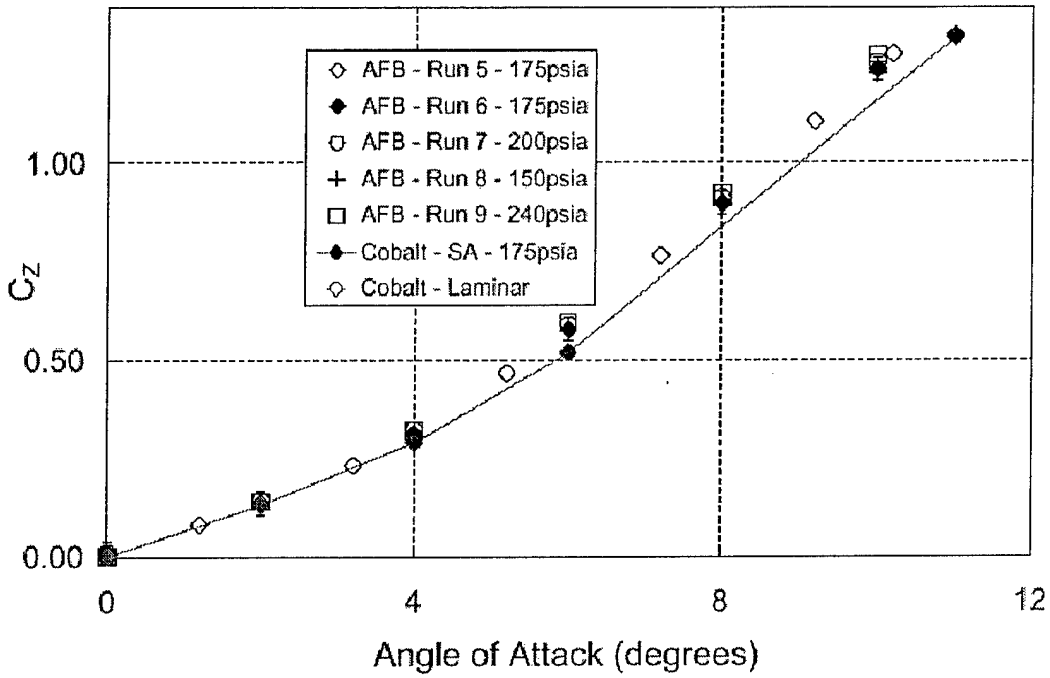

Figure 34. Normal force for an H3 model

The experimentally-determined axial force coefficients, $C_{X,eff}$, for the baseline model built at the USAFA (AFB) are compared with the computed values in Figure 35. The computed axial force component assumes that the pressure acting on the base of the model is equal to the free-stream static pressure. Therefore, in order to allow a direct comparison between the experimentally determined axial force coefficients and the computed values, it is necessary to apply a correction to the to the experimental results.

The axial force, X, that is measured by the force balance, is the difference between the net force acting on the forward facing surfaces, X_{fore}, and the force acting on the base of the model. During the force-and-moment tests, two static pressure probes were located adjacent to the model-support sting in the base region of the model. Averaging the pressures sensed by these two probes yields an average value for the experimental base pressure, $P_{b,ave}$. The area over which the average value of the two base-pressure measurements acts is assumed to be the total base area of the model, S. Therefore, X is given by the following equation:

$$X = X_{fore} - P_{b,ave}S \tag{8}$$

Therefore, it is possible to calculate the force acting only on the forward facing surface of the model:

$$X_{fore} = X + P_{b,ave}S \tag{9}$$

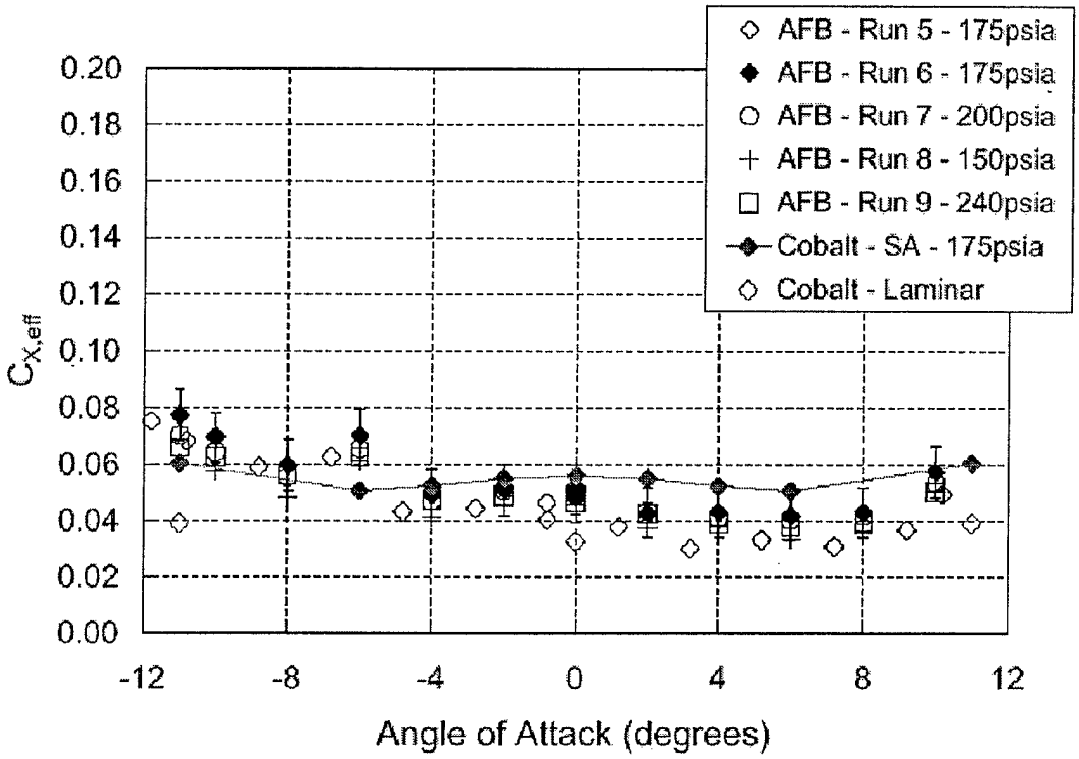

Figure 35. Effective axial force for an H3 model

Instead of using the average value of the two base-pressure measurements to calculate the force acting on the base of the model, let us assume that the free-static pressure acts on the base of the model. Assuming that P_1 acts on the base of the model, the effective axial force, X_{eff}, is equal to the force that would act on the base due to the free-stream static pressure subtracted from the force acting on the forebody and is given as follows:

$$X_{eff} = X_{fore} - P_1 S \tag{10}$$

The effective axial force coefficient can then be calculated as follows:

$$C_{X,eff} = \frac{X_{eff}}{q_1 S} \tag{11}$$

The experimental values of the effective axial force coefficient as determined using equation (11), are presented in Figure 35. Experimentally-determined values of $C_{X,eff}$ are presented for all four Reynolds numbers (i.e., all four values of the stilling chamber pressure). Measurements from two runs at a Reynolds number Re_L of approximately 13.69×10^6 (or $P_{t1} = 175\ psia$) are in good agreement at the large negative angles-of-attack, but differ significantly as the angle-of-attack is increased. Recall that the stilling chamber pressure is held constant during a run. Furthermore, the force-and-

moment measurements for a given angle-of-attack are recorded while the model pauses at the desired angle-of-attack during an alpha sweep. Note that the angle-of-attack for the measurements from Run 5 are offset 0.8° from all of the other data. Since the offset angle was measured before and/or after a run, this large offset indicates that the angle-of-attack changed significantly during this run. The angle-of-attack sequence for which the data of run 5 were obtained, started at a control input value of zero, swept to -11°, went to +11°, and then swept back to zero. Thus, the data from the alpha points early in the sequence (the negative angles-of-attack) are in relatively good agreement with the data from Run 6. The differences between the Run 5 measurements and the Run 6 measurements are greater for the data from the alpha points late in the sequence (the positive angles-of-attack). Because of the time-dependent nature of the differences between the data from Run 5 and those from Run 6 and because of the relatively large offset angle, the authors believe that the model was not properly mounted for Run 5 and the data from this run are considered anomalous.

The values of the effective axial force coefficient, as computed using the Cobalt_{60} code, are included in Figure 35. Computations are presented for two boundary-layer models: (1) the boundary layer is entirely laminar and (2) the boundary layer is entirely turbulent using the Spalart and Allmaras turbulence model[25]. As would be expected for this slender body operating at relatively low angles-of-attack, the laminar values for $C_{x,eff}$ are significantly less than the turbulent values. The values of $C_{x,eff}$ that were computed assuming the boundary layer was wholly turbulent decrease slightly as the absolute value of the angle-of-attack goes from zero to six degrees, where it is a minimum. The effective axial force coefficient then increases with alpha. This angle-of-attack dependence for $C_{x,eff}$, first decreasing with alpha to a minimum, then increasing with alpha is believed to reflect the changing role of the skin-friction component of drag relative to the form drag component.

With the exception of the data obtained at an angle-of-attack of -6°, the experimentally-determined values of the effective axial force coefficient, $C_{x,eff}$, for negative angles-of-attack agree closely with the computations for the wholly turbulent boundary layer, both in magnitude and in their angle-of-attack dependence. For positive angles-of-attack, the alpha dependence of the experimentally determined values of $C_{x,eff}$ is similar to that for the turbulent computations. However, the experimentally determined values are less than the computed values assuming that the boundary layer is wholly turbulent. Thus, the experimental values of $C_{x,eff}$ exhibit an asymmetry between the data obtained at positive and negative angles-of-attack. For some of the runs, the two base pressure measurements were approximately equal, both in magnitude and in alpha dependence. For other runs, the two base pressure measurements were significantly different at certain angles-of-attack. Thus, the authors believe that a significant contributor to the difference between the experimentally-determined value of $C_{x,eff}$ at a given positive angles-of-attack and its value at the corresponding negative angle-of-attack is due to an anomaly in the base-pressure measurements.

The pitching moment coefficient about the apex is presented as a function of the positive angles-of-attack in Figure 36 for all four Reynolds numbers. The measured

values for the pitching moment coefficient are independent of the Reynolds number over the range for which data were obtained. Included for comparison are the pitching moment coefficients computed using the $Cobalt_{60}$ code. CFD solutions were obtained under the assumption that the boundary layer was fully laminar or that it was fully turbulent, using the turbulence model of Spalart and Allmaras[25]. The differences between the experimentally determined pitching moment coefficients and those computed assuming that the boundary layer is fully turbulent, although small, increase with alpha. Although the boundary layer is believed to be turbulent at the high Reynolds numbers associated with this study, the pitching moment coefficients computed assuming the boundary layer is wholly laminar are in relatively good agreement with the experimental values at 11°.

The movement of the center of pressure with angle-of-attack for the baseline model is presented in Figure 37. The center of pressure is located at just over $x/L = 0.5$ and x_{cp}/L increases slightly as the magnitude of the angle-of-attack increases. This is in good agreement with the results of Edwards and Roper[10], which indicated the center of pressure was at a position of $x/L = 0.56$.

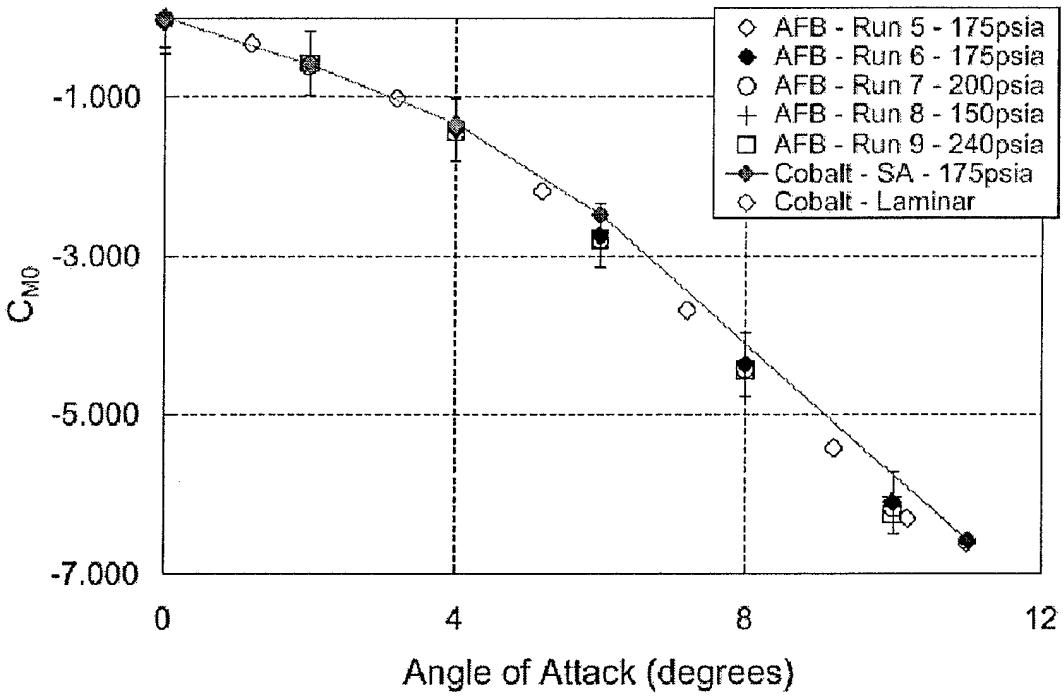

Figure 36. Pitching moment coefficient around the apex for the AFB model as a function of alpha

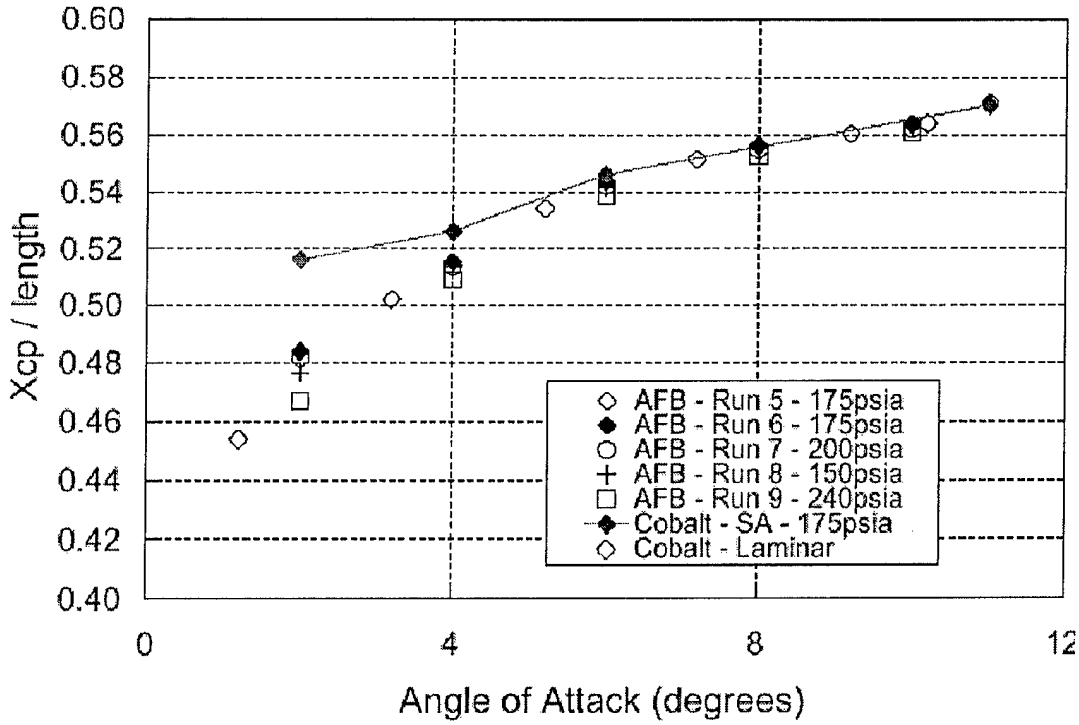

Figure 37. The location of the center of pressure as a function of alpha

2. Free Flight Data

For all coefficients and derivatives, the reference length is the major ellipse diameter (d_{maj}) of the base and the reference area is the cross section area of the model base ($A=\pi*(d_{maj}*d_{min})/4$). The moment reference point is about the center of gravity (46.6% from the nose). The complete set of aerodynamic data from the experiments and predictions are presented in Table 7. For the $Cobalt_{60}$ data, the forces and moments were a result of surface integration of the pressure and shear stress.

The zero yaw axial force coefficient (C_{X_o}) versus Mach number is shown in Figure 38. The shaded symbols are the result of matching multiple flight trajectories to a common set of aerodynamics. Figure 38 shows good agreement between the experimental data and the predictions. The base drag is the dominant drag for a slender projectile such as the H3, therefore, predicting the base pressure is crucial to accurately predicting the drag. For the Mach 2.5 base flow previously examined[30], turbulence models without compressibility corrections were seen to under-predict the base pressure by 40-90%. Menter's Baseline model with compressibility corrections (the model used in the current study) predicted the base pressure to within 12%. The good agreement in the current research is probably in large part due to the proper choice of turbulence models.

Figure 39 shows the normal force coefficient derivative in the pitch plane ($C_{Z\alpha}$) versus Mach number. Figure 40 shows the yaw plane normal force coefficient derivative ($C_{Y\beta}$) versus Mach number. A fair amount of scatter is immediately seen in the

experimentally-determined values for normal/yaw force derivative. This coefficient is sometimes difficult to measure accurately from free-flight data if there is not sufficient heaving motion of the projectile[16], as in this case. Better agreement is seen with multiple-fit data for this derivative. The aeroprediction data (AP98) and CFD data appear agree very well in the Mach number range shown.

Figure 41 contains the pitching moment coefficient derivative in the pitch plane ($C_{m\alpha}$) as a function of Mach number. Similarly, the yaw plane moment coefficient derivative ($C_{n\beta}$) versus Mach number is shown in Figure 42. There is more consistency in this data versus the force data. Again, this is in general the situation where the angular data is measured well within the free-flight range.

It is seen from the moment data that the H3 configuration is marginally stable and that there is little variation with Mach number. In spite of this marginal stability, there was very little angular motion observed in the experimental data. As seen from the total angle of attack data ($\overline{\alpha}^2$) in Table 7, the angle of attack was only a few degrees, at most (with the exception of shot 54). Predictions of the moment data agree very well with that of the observed data. However, they predict slightly more moment stability in both the pitch and yaw planes.

Table 7. Aerodynamic Results

	air density (kg/m^3)	Speed of sound (m/s)	Mach number	C_{X_0}	$C_{Z\alpha}$	$C_{Y\beta}$	$C_{m\alpha}$	$C_{n\beta}$	X_{cp}/l	$\overline{\alpha}^2$	shot number
Aeroprediction Code (AP98)											
	1.2256	340.27	1.30	0.307	3.566	1.274	-1.291	-0.793	0.506		
	1.2256	340.27	2.00	0.222	3.624	1.294	-1.094	-0.706	0.500		
	1.2256	340.27	3.00	0.158	3.708	1.317	-1.091	-0.697	0.499		
	1.2256	340.27	4.00	0.120	3.744	1.330	-1.156	-0.735	0.500		
	1.2256	340.27	4.28	0.111	3.749	1.332	-1.175	-0.745	0.501		
	1.2256	340.27	5.00	0.092	3.756	1.334	-1.218	-0.774	0.502		
	1.2256	340.27	6.00	0.076	3.387	1.235	-1.174	-0.984	0.505		
	1.2256	340.27	7.00	0.065	3.385	1.233	-1.163	-0.919	0.504		
Free-Flight Range (ARF)											
single fits	1.206	343.7	3.00	0.200	4.170	1.640	-0.953	-0.349	0.474	0.6	*66*
	1.209	343.0	3.32	0.156	3.720	1.210	-1.061	-0.542	0.476	2.7	*67*
	1.205	344.1	3.65	0.151	3.200	2.310	-0.992	-0.782	0.476	2.2	*65*
	1.196	344.2	3.98	0.130	3.490	2.120	-0.899	-0.651	0.475	7.8	*56*
	1.207	344.3	4.14	0.112	4.870	1.130	-0.914	-0.418	0.472	3.0	*63*
	1.201	344.6	4.18	0.133	3.560	1.610	-1.356	-0.635	0.479	3.1	*64*
	1.209	343.7	4.36	0.119	2.430	1.490	-1.526	-0.511	0.487	0.3	*62*
	1.209	343.6	4.50	0.109	3.070	1.850	-0.992	-0.767	0.477	2.2	*61*
	1.196	344.2	4.92	0.104	3.750	1.980	-1.580	-0.682	0.480	11.2	*54*
multiple fits			3.16	0.178	4.270	1.190	-1.286	-0.434	0.476	1.6	*66, 67*
			3.82	0.149	3.320	2.220	-0.821	-0.674	0.474	5.0	*65, 56*
			4.27	0.126	2.990	1.460	-1.557	-0.503	0.483	1.8	*62, 64*
			4.71	0.106	3.570	2.110	-1.061	-0.449	0.476	6.9	*61, 54*
Cobalt$_{60}$											
	1.2256	343.86	4.20	0.107	3.510	1.520	-1.362*	-0.569*	0.522		

* based upon solutions at 0 & 1 degrees α

Figure 43 presents the center of pressure variation with Mach number for this configuration as observed from the data. The center of pressure location for the data of Figure 43 were found via equation (12)[16], given as:

$$\frac{X_{c.p.}}{L} = \frac{X_{CG}}{L} - \frac{C_{m\alpha}}{C_{Z\alpha}} \frac{d_{maj}}{L}. \tag{12}$$

Here it is seen that the experimental data has a center of pressure slightly ahead of the predicted values. As can be seen here, the test configuration was just slightly stable. The computational location for the center of pressure is slightly aft of both the free-flight data and the AP98 data.

Pitch damping (C_{mq}) and yaw damping ($C_{n\beta}$) were not adequately determined from the free-flight data due to the small amplitude changes during each flight in the ARF. Trim asymmetries and roll induced side moments resulted in a complex motion spectrum. A representative value for pitch damping is believed to be about *–50.*

Figure 44 shows a direct shadowgraph of the H3 projectile obtained in the ARF. This shadowgraph is from shot 67 (Mach 3.32) and shows the shock structure and wake region in more detail.

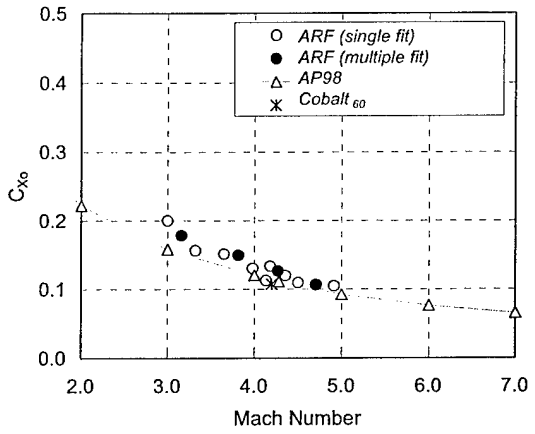

Figure 38. Zero-yaw axial force coefficient vs. Mach number

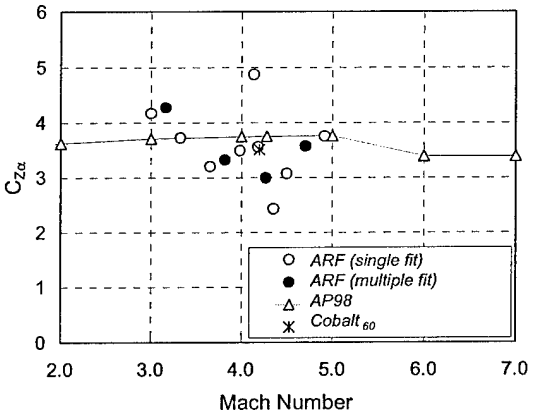

Figure 39. Pitch plane normal force coefficient derivative vs. Mach number

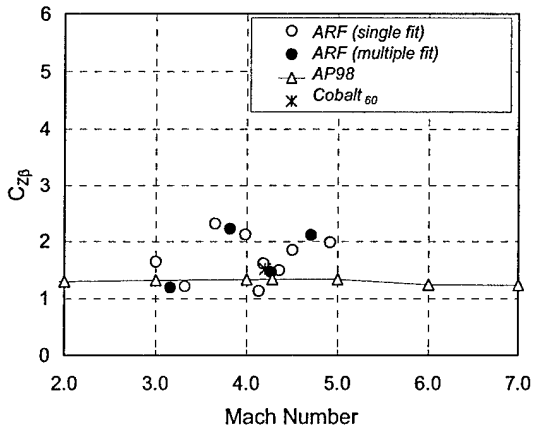

Figure 40. Yaw plane normal force coefficient derivative vs. Mach number

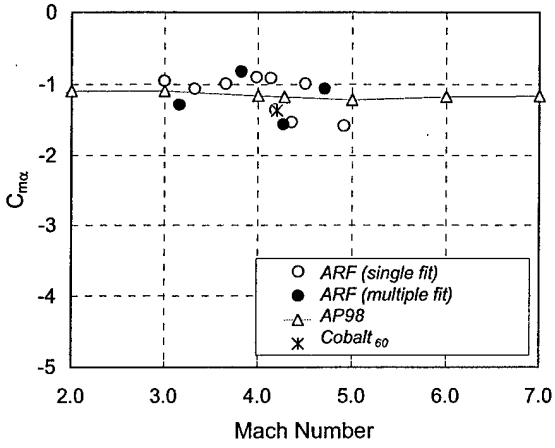

Figure 41. Pitch plane moment coefficient derivative vs. Mach number

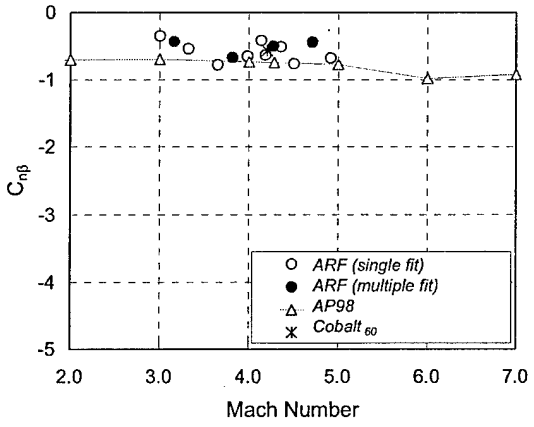

Figure 42. Yaw plane moment coefficient derivative vs. Mach number

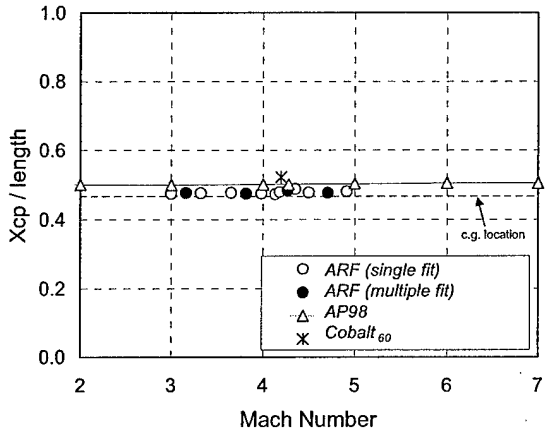

Figure 43. Center of pressure variation vs. Mach number

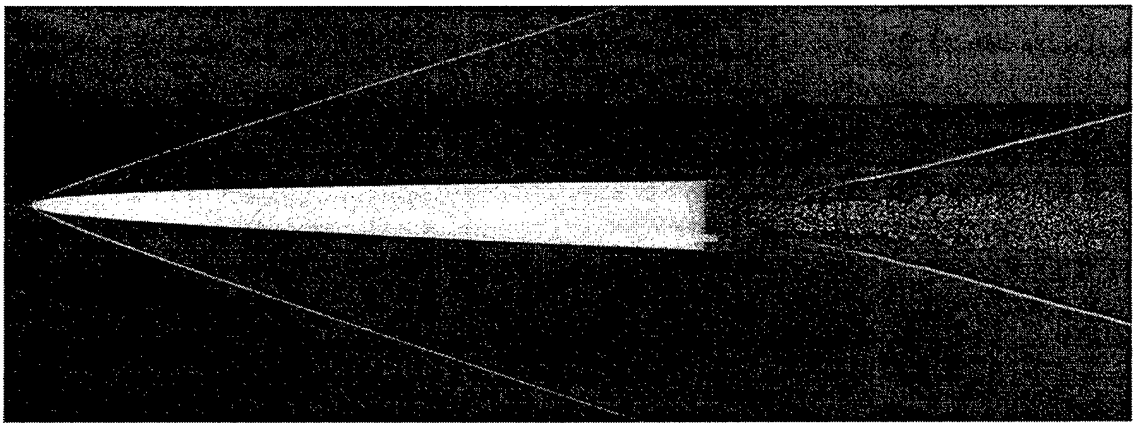

Figure 44 Shadowgraph of H3 projectile traveling at Mach 3.32 (shot 67)

THIS PAGE INTENTIONALLY LEFT BLANK

SECTION VI

CONCLUSIONS

1. Wind Tunnel Data

The following conclusions can be drawn regarding the flow field, based on the experimental data and on the flow-field computations discussed in the present report over the range of conditions studied.

- The zero-angle-of-attack pressure measurements from the top surface and from the bottom surface follow a single, well-behaved curve at each station, both in magnitude and in their dependence on y. Thus, the experimentally determined pressure measurements indicate that both the model and the wind-tunnel flow field are symmetric about the xy-plane, i.e., the yaw plane.

- For a given value of y/y_{max}, the pressure measured in the upstream plane, i.e., at $x = 4.50$ *inches*, is slightly greater than the pressure measured in the downstream plane, i.e., at $x = 9.00$ *inches*. This is true for both the measured pressures and for the computed pressures. This should be expected since the local surface inclination angle decreases with distance from the apex of the model.

- The normal force coefficient is a linear function of the angle-of-attack for values of alpha in the range $\pm 4^{\circ}$. The components of the velocity vectors taken from the $Cobalt_{60}$ computed flow field for a plane of constant x indicate cross-flow separation (i.e., a free-vortex shear-layer separation, occurs at an angle-of-attack of 6°). Over the entire angle-of-attack range for which data were obtained, the normal force coefficients, the pitching moment coefficients, and the center of pressure locations were independent of the Reynolds number, or equivalently, the total pressure in the stilling chamber.

- The effective axial force coefficients are significantly affected by the Reynolds number. Values of the effective axial force coefficient from the flow fields computed using the $Cobalt_{60}$ code were significantly greater, when the boundary layer is assumed to be fully turbulent as compared to the computations made assuming that the boundary layer remains laminar along its entire length.

- Oil-flow patterns that were observed on the surface of the baseline model at an angle-of-attack of 10° indicate a more complex flow field than was evident in the computed solution. Oil-flow patterns indicate the existence both of a primary- and of a secondary-separation location. The primary-separation location occurred very near

the yaw plane as the flow proceeded from the windward surface around the rapid change in cross-section slope for large values of y. The components of the velocity vectors taken from the $Cobalt_{60}$ computed flow field for a plane of constant x indicate a single cross-flow separation, that is produced by the free-vortex shear-layer separation.

2. Free Flight Data

Free-flight experiments of a power-law elliptic cross-section projectile have been conducted and analyzed from Mach numbers of 3.0 through 5.0. Aerodynamic stability derivatives and coefficients have been determined from this data. Computational fluid dynamic simulations were run at the Mach 4.2 free-flight conditions and have been compared to the experimental data. The experimental and CFD data were compared with results from an engineering level aeroprediction code (AP98).

Overall, the agreement between the force and moment coefficients of the numerical method ($Cobalt_{60}$) and engineering method (AP98) with the measurements obtained in the free-flight range is good. This builds confidence in these methods as useful predictive tools for this and similar configurations for preliminary design. To truly validate these tools for an in-depth detailed design study, a grid refinement study would need to be accomplished for the CFD. Additionally, higher amplitude motion would need to be induced in the free-flight projectiles to provide experimental data at higher angles of attack. This will allow better determination of aerodynamic coefficients and stability derivatives. This will reduce the scatter seen in free-flight results and allow the nonlinear behavior of the coefficients to be determined.

AP98, an empirical based method, was highly efficient, taking only minutes to setup and run a case. Further, AP98 was able to predict the aerodynamics of the H3 reasonably well. $Cobalt_{60}$ complements AP98 since it is able to handle complex geometries through the use of unstructured grids. Solutions take longer, however, with about one day to create the grid, and one day per solution. The advantage of using CFD methods is to predict the entire flowfield, which includes complex phenomena. These can include separated flow and shock/vortex interaction.

As encouraging as these results are, there was a discrepancy between the prediction methods and free-flight results for the center of pressure, the most crucial parameter to predict. A maneuvering projectile would require its center of gravity forward of the center of pressure for stability, but not so far forward as to reduce maneuverability. Grid refinement in the CFD may have reduced this discrepancy.

APPENDIX A – NOMENCLATURE

$\overline{\alpha}$ = Total angle of attack

$\overline{q}$ = Dynamic pressure

6DOF = Six degree of freedom

A = Cross section area of the model and reference area ($A=\pi*(d_{maj}*d_{min})/4$)

a, d_{maj} = Major axis dimension (total width) at the base

AFB = Air Force Base

AFB = USAFA produced Force/Moment Baseline model

AFM = USAFA produced Force/Moment Modified baseline model

AFRL = Air Force Research Laboratory

APB = USAFA produced Pressure Baseline model

APM = USAFA produced Pressure Modified baseline model

ARF = Aeroballistic Research Facility

ARFDAS = Aeroballistic Research Facility Data Analysis System

b, d_{min} = Minor-axis dimension (total width) at the base

C_1, C_2 = Body geometry contestants

CADRA = Comprehensive Aerodynamic Data Reduction Analysis

CFD = Computational fluid dynamics

CG, cg = Center of gravity

C_l = Roll moment coefficient ($C_l \equiv \frac{l}{\overline{q}Ad_{ref}}$)

C_m = Pitch moment coefficient ($C_m \equiv \frac{m}{\overline{q}Ad_{ref}}$)

C_{mo} = Pitching moment coefficient about the apex of the model

C_{mq} = Pitch damping moment coefficient derivative ($\frac{\partial Cm}{\partial q}$)

$C_{m\alpha}$ = Pitching moment coefficient derivative ($\frac{\partial Cm}{\partial \alpha}$)

C_n = Yaw moment coefficient ($C_n \equiv \frac{n}{\overline{q}Ad_{ref}}$)

C_{nr} = Yaw damping moment coefficient derivative ($\frac{\partial Cn}{\partial r}$)

$C_{n\beta}$ = Yaw moment coefficient derivative ($\frac{\partial Cn}{\partial \beta}$)

C_X = Axial force coefficient ($C_X \equiv \frac{X}{\overline{q}A}$)

C_{Xo} = Zero yaw axial force coefficient

C_Y = Yaw force coefficient ($C_Y \equiv \frac{Y}{\overline{q}A}$)

$C_{Y\beta}$ = Normal force coefficient derivative in the yaw plane ($\frac{\partial C_Y}{\partial \beta}$)

C_Z = Normal force coefficient ($C_Z \equiv \frac{Z}{\overline{q}A}$)

C_Z = Normal force coefficient

$C_{Z\alpha}$ = Normal force coefficient derivative in the pitch plane ($\frac{\partial C_Z}{\partial \alpha}$)

d_{ref}	=	Reference diameter of the model
e	=	Elliptic cross-section eccentricity
EFB	=	Eglin AFB produced Force/Moment Baseline model
EPB	=	Eglin AFB produced Pressure Baseline model
HPCF	=	High-Performance Computing Facility
I_x, I_y	=	Moment of inertia about the x and y axis
k	=	Model surface constant
L	=	Model length
l,m,n	=	Roll, pitch, and yaw moment about projectile cg
L_{ref}	=	Reference length in the definition of the pitching-moment coefficient (= a, the dimension of the major axis at the base)
M, M_1	=	Free-stream Mach number
mbar	=	milibar
MLM	=	Maximum Likelihood Method
M_o	=	Pitching moment about the apex of the model
NSWC	=	Naval Air Warfare Center
^oC	=	Celsius
^oF	=	Degrees Fahrenheit
^oR	=	Degrees Rankine
P	=	Static pressure
p,q,r	=	Roll rate, pitch rate, and yaw rate about projectile cg
P_1	=	Free-stream static pressure
$P_{b,ave}$	=	Average value of the two measurements of the static pressure in the base region of the model
PLES	=	Power law elliptic section
PNS	=	Parabolized Navier-Stokes
psia	=	Pounds per square inch absolute
P_{t1}	=	Total pressure in the tunnel stagnation chamber, also P_{t1}
q_1	=	Free-stream dynamic pressure, $(\gamma/2)P_1M_1^2$
r	=	Radius of model surface
Re_L	=	Reynolds number, based on the free-stream conditions and the model length
S	=	Model base area, $\pi ab/4$
S/HABP	=	Supersonic/Hypersonic Arbitrary Body Program
SOSE	=	Second-order shock-expansion
T_{t1}	=	Total temperature in the tunnel stagnation chamber
TWT	=	Tri-sonic Wind Tunnel
USAF	=	United States Air Force
USAFA	=	United States Air Force Academy
V	=	Volts
x	=	Axial coordinate
x,y,z	=	Downrange, side, and vertical position coordinates
X,Y,Z	=	Axial, yaw, and normal body forces
$X_{c.p.}$	=	Location of center of pressure measured from nose
X_{CG}	=	Location of center of gravity measured from nose
y_{max}	=	Maximum value of the y-coordinate at a given x-station

z_{max} = Maximum value of the z-coordinate at a given x-station

α = Pitch angle

β = Yaw angle

ϕ = Roll angle, or model axial rotation, $\phi = 0^{\circ}$ corresponds to the negative z-side of the xz-plane; $\phi = 270^{\circ}$ corresponds to the positive y-side of the xy plane

γ = Ratio of specific heats, 1.4 for perfect air

θ = Angular coordinate of model surface

INTENTIONALLY LEFT BLANK

APPENDIX B – BODY FIXED AERODYNAMIC MODEL

1. 6DOF – Methodology

The aerodynamic data presented in this report that were obtained using the "body fixed" 6DOF analysis is detailed in this appendix. Here, the equations of motion are derived with respect to a rotating body fixed coordinate system. The *x*-axis points down the axis of the body, the *y*-axis points out the left side of the body looking downrange, and the *z*-axis points up with respect to the body. The body fixed coordinate system is rigidly affixed to the projectile and rotates with the body about the *x*-axis. The inertial frame of reference is the earth. It is assumed the earth is fixed in space and flat. The body fixed equations of motion are given as follows where the subscript "*b*" refers to the body fixed coordinate system.

BODY FIXED EQUATIONS OF MOTION

$$\dot{u}_b = g\sin\theta - q_b w_b + r_b v_b - a_{cub} + \frac{F_{xb}}{\overline{m}}$$

$$\dot{v}_b = p_b w_b - r_b u_b - g\sin\phi\cos\theta - a_{cvb} + \frac{F_{yb}}{\overline{m}}$$

$$\dot{w}_b = q_b u_b - p_b v_b - g\cos\phi\cos\theta - a_{cwb} + \frac{F_{zb}}{\overline{m}}$$

$$\dot{p}_b = \frac{I_y l_b + I_{xy} m_b - (I_x + I_y - I_z) I_{xy} p_b r_b + (I_{xy}^2 + I_y(I_y - I_z)) q_b r_b}{(I_x I_y - I_{xy}^2)}$$

$$\dot{q}_b = \frac{I_x m_b + I_{xy} l_b + (I_x + I_y - I_z) I_{xy} q_b r_b + (I_x(I_z - I_x) - I_{xy}^2) p_b r_b}{(I_x I_y - I_{xy}^2)}$$

$$\dot{r}_b = \frac{n_b + I_{xy}(p_b^2 - q_b^2) + (I_x - I_y) p_b q_b}{I_z}$$

Where a_{cub}, a_{cvb}, *and* a_{cwb} are coriolis accelerations dependent on the latitude λ_R and azimuth δ_R of the range and rotational rate of the earth ω_e.

BODY FIXED CORIOLIS ACCELERATIONS

$$
\begin{aligned}
a_{cx} &= -2\omega_e(\dot{y}\sin\lambda_R + \dot{z}\cos\lambda_R\sin\delta_R)\\
a_{cy} &= +2\omega_e(\dot{x}\sin\lambda_R - \dot{z}\cos\lambda_R\cos\delta_R)\\
a_{cz} &= +2\omega_e(\dot{x}\cos\lambda_R\sin\delta_R + \dot{y}\cos\lambda_R\cos\delta_R)\\
a_{cub} &= a_{cx}\cos\theta\cos\psi + a_{cy}\cos\theta\sin\psi - a_{cz}\sin\theta\\
a_{cvb} &= a_{cx}(\sin\theta\sin\phi\cos\psi - \cos\phi\sin\psi) + a_{cy}(\sin\theta\sin\phi\sin\psi + \cos\phi\cos\psi)\\
&\quad + a_{cz}(\sin\phi\cos\theta)\\
a_{cwb} &= a_{cx}(\sin\theta\cos\psi\cos\phi + \sin\phi\sin\psi) + a_{cy}(\sin\theta\cos\phi\sin\psi - \sin\phi\cos\psi)\\
&\quad + a_{cz}(\cos\phi\cos\theta)
\end{aligned}
$$

Once the aerodynamic forces and moments (i.e., F_x, F_y, F_z, l, m, n) are determined, the solution of the body fixed equations of motion will define the 6DOF flight motion with respect to the body fixed coordinate system. Since the position-attitude measurements, as acquired from the ballistic spark range, are relative to the Earth-fixed coordinate system, additional transformation equations are required. These transformation equations are shown below in terms of the fixed plane Euler angles (θ, ψ) and the angle of rotation about the missile axis (ϕ).

EARTH FIXED TRANSFORMATION EQUATIONS (BODY FIXED)

$$
\begin{aligned}
\dot{x} &= u_b\cos\theta\cos\psi + v_b(\sin\theta\sin\phi\cos\psi + \cos\phi\sin\psi)\\
&\quad + w_b(\sin\theta\cos\phi\cos\psi + \sin\phi\sin\psi)\\
\dot{y} &= u_b\cos\theta\sin\psi + v_b(\sin\theta\sin\phi\sin\psi + \cos\phi\cos\psi)\\
&\quad + w_b(\sin\theta\cos\phi\sin\psi - \sin\phi\cos\psi)\\
\dot{z} &= -u_b\sin\theta + v_b\cos\theta\sin\phi\\
&\quad + w\cos\theta\cos\phi\\
\dot{\theta} &= q_b\cos\phi - r_b\sin\phi\\
\dot{\psi} &= \frac{q_b\sin\phi + r_b\cos\phi}{\cos\theta}\\
\dot{\phi} &= p_b + \tan\theta(q_b\sin\phi + r_b\cos\phi)
\end{aligned}
$$

The Equations of Motion and the Earth Fixed Transformation Equations are numerically integrated using a fourth-order Runge-Kutta scheme.

2. Aerodynamic Forces and Moments.

The body fixed aerodynamic forces and moments are defined as follows:

$$F_{xb} = -\bar{q}A\overline{C}_X$$

$$F_{yb} = \bar{q}A[-\overline{C}_{Y0} - \overline{C}_{Y\beta}\frac{v_b}{V} + \frac{p_b d}{2V}\overline{C}_{Yp\alpha}\frac{w_b}{V} + \overline{C}_{Y\gamma\alpha}\frac{w_b}{V}]$$

$$F_{zb} = \bar{q}A[-\overline{C}_{Z0} - \overline{C}_{Z\alpha}\frac{w_b}{V} - \frac{p_b d}{2V}\overline{C}_{Yp\alpha}\frac{v_b}{V} - \overline{C}_{Y\gamma\alpha}\frac{v_b}{V}]$$

$$l_b = \bar{q}A[\frac{p_b d}{2V}\overline{C}_{\ell p} + C_{\ell\delta}\delta + \overline{C}_{\ell\gamma\alpha}]$$

$$m_b = \bar{q}Ad[C_{m0} + \overline{C}_{m\alpha}\frac{w_b}{V} + \frac{q_b d}{2V}\overline{C}_{mq} + \frac{p_b d}{2V}\overline{C}_{np\alpha}\frac{v_b}{V} + \overline{C}_{n\gamma\alpha}\frac{v_b}{V}]$$

$$n_b = \bar{q}Ad[-C_{n0} - \overline{C}_{n\beta}\frac{v_b}{V} + \frac{r_b d}{2V}\overline{C}_{nr} + \frac{p_b d}{2V}\overline{C}_{np\alpha}\frac{w_b}{V} + \overline{C}_{n\gamma\alpha}\frac{w_b}{V}]$$

where:

A = reference area

d = reference length

$\bar{q}$ = dynamic pressure $= \frac{1}{2}\rho V^2$

$V = \sqrt{u_b^2 + v_b^2 + w_b^2}$

The aerodynamic coefficients and derivatives are assumed to be nonlinear functions of Mach number, sine of the total angle of attack, and the aerodynamic roll angle. This assumption is made in a general sense in defining a generalized aerodynamic math model. These expansion for the body fixed equations of motion are shown as follows:

AERODYNAMIC COEFFICIENT EXPANSIONS (BODY FIXED)

Axial Force Coefficient

$$\overline{C}_X = C_{XO} + C_{X\alpha_2}(\frac{w_b}{V})^2 + C_{X\beta_2}(\frac{v_b}{V})^2 + C_{Xm}(M_i - M_r) + C_{X\gamma\alpha_2}\varepsilon^2\cos N\gamma$$

Normal Force Coefficient Derivative

$$\overline{C}_{Z\alpha} = C_{Z\alpha} + C_{Z\alpha_3}(\frac{w_b}{V})^2 + C_{N\gamma\alpha_3}\varepsilon^2\cos N_\gamma$$

Side Force Coefficient Derivative

$$\overline{C}_{Y\beta} = C_{Y\beta} + C_{Y\beta_3}(\frac{v_b}{V})^2 + C_{N\gamma\alpha_3}\varepsilon^2 \cos N\gamma$$

Magnus Force Coefficient Derivative

$$\overline{C}_{Yp\alpha} = C_{Yp\alpha}$$

Induced Side Force Coefficient

$$\overline{C}_{Y\gamma\alpha} = C_{Y\gamma\alpha_3}\varepsilon^2 \sin N\gamma$$

Spin Decay Roll Moment Coefficient

$$\overline{C}_{\ell p} = C_{\ell p} + C_{\ell p\alpha_2}\varepsilon^2 + C_{\ell pm}(M_i - M_r)$$

Static/Induced Roll Moment Coefficient

$$\overline{C}_{\ell} = C_{\ell\delta}\delta + C_{\ell\gamma\alpha_2} \sin N\gamma$$

Pitching Moment Coefficient Derivative

$$\overline{C}_{m\alpha} = C_{m\alpha} + C_{m\alpha_3}(\frac{w_b}{V})^2 + C_{Z\alpha}(CG - CG_r) + C_{m\gamma\alpha_3}\varepsilon^2 \cos N\gamma$$

Yawing Moment Coefficient Derivative

$$\overline{C}_{n\beta} = C_{n\beta} + C_{n\beta_3}(\frac{v_b}{V})^2 + C_{Y\beta}(CG - CG_r) + C_{m\gamma\alpha_3}\varepsilon^2 \cos N\gamma$$

Pitch Damping Moment Coefficient

$$\overline{C}_{mq} = C_{mq} + C_{mq\alpha_2}(\frac{w_b}{V})^2$$

Yaw Damping Moment Coefficient

$$\overline{C}_{nr} = C_{nr} + C_{nr\alpha_2}(\frac{v_b}{V})^2$$

Magnus Moment Coefficient Derivative

$$\overline{C}_{np\alpha} = C_{np\alpha}$$

Induced Side Moment Coefficient Derivative

$$\overline{C}_{n\gamma\alpha} = C_{n\gamma\alpha_3}\varepsilon^2 \sin N_\gamma + C_{n\gamma\alpha_5}\varepsilon^4 \sin N_\gamma$$

Trim Force Coefficients

$$\overline{C}_{Z0}, \overline{C}_{Y0}$$

Trim Moment Coefficients

$$\overline{C}_{m0}, \overline{C}_{n0}$$

The aerodynamic roll angle, γ, is computed as follows:

$$\gamma = \tan^{-1}(v_b / w_b)$$

The sine of the total angle of attack is calculated as follows:

$$\varepsilon = \sqrt{\frac{v^2 + w^2}{V}}$$

The body fixed pitch and yaw angles are defined as follows:

$$\alpha = \frac{w_b}{V}$$

$$\beta = \frac{v_b}{V}$$

Slight variations in the center of gravity (CG) between test projectiles (models) are accounted for by assigning a reference CG location (CG_r) and making an appropriate correction to the pitching moment coefficient derivative. The pitching moment coefficient is the only coefficient of which slight changes in CG have a first order effect on the observed motion.

The full 6DOF equations of motion portion of the analysis eliminates the assumptions of Linear Theory by retaining all cross coupling terms and allowing nonlinearities both as functions of Mach number and angle of attack. In addition, the procedure within ARFDAS allows analysis of up to five test flights simultaneously. This provides improved accuracy of the extracted aerodynamics and their nonlinearities with angle-of-attack, roll angle, and Mach number.

INTENTIONALLY LEFT BLANK

REFERENCES

1 Kontis, K., Stollery, J. L., and Edwards, J. A., "Hyper-sonic Effectiveness of Slender Lifting Elliptic Cones With and Without Strakes," AIAA Paper 97{0521, Jan. 1997, Presented at the 35th Aerospace Sciences Meeting and Exhibit, Reno, NV.

2 Bertin, J. J., Hypersonic Aerothermodynamics, AIAA Education Series, Washington, D.C., 1994.

3 Pagan, D., Molton, P., and Delery, J., \Basic Experiment on a Supersonic Vortex Flow Around a Missile Body," Journal of Spacecraft and Rockets, Vol. 29,No. 3, May 1992, pp. 373-378.

4 Moore, F. G. and Hymer, T. C., \Semiempirical Prediction of Pitch Damping Moments for Configurations with Flares," Journal of Spacecraft and Rockets, Vol. 38, No. 2, March 2001, pp. 50-58.

5 Sigal, A., "Methods of Analysis and Experiments for Missiles with Noncircular Fuselages," Tactical Missile Aerodynamics, Prediction Methodology, edited by M. R. Mendenhall, AIAA, 2nd ed., 1992.

6 Kontis, K., Qin, N., and Stollery, J.L., "Computational and Experimental Investigation of Hypersonic Performance of a Lifting Elliptic Cone With and Without Strakes," AIAA Paper 97-2252, 1997.

7 Grasso, F. and Iaccarino, G., "Influence of Crossflow and Turbulence on Vortex Flow Around a Supersonic Missile," Journal of Spacecraft and Rockets, Vol. 35, No. 1, Jan.-Feb. 1998, pp. 37-45.

8 Shereda, R. E., Amidon, P. F., and Dahlem, V. I., "Wind Tunnel Tests of Elliptical Missile Body Configurations at Mach Numbers 0.4 to 5.0," AFWAL-TR 87-3086, Dec. 1987.

9 Shepherd, P. A. and Tod, J. R., \Development and Application of a Weapons Multiblock Suite," AGARD CP-473, May 1988, Presented at Symposium on Fluid Dynamics, Lisbon, Portugal.

10 Edwards, J. A. and Roper, J. J., \A Computational Assessment of Static and Dynamic Coefficients for the H3 Hypervelocity Projectile," AIAA Paper 97-0640, Jan. 1997.

11 Pesek, T. W., Bertin, J. J., Forsythe, J. R., Pluntze, S. C., Schuricht, P. H., and Abate, G., "Supersonic Flowfield for a Slender, Power-Law Elliptic-Section (PLES) Projectile," AIAA Paper 2000-0120, Jan. 2000.

12 Schuricht, P. H.,Forsythe, J. R., Bertin, J. J., , and Abate, G. L., "Comparison Between Measurements and Computations for Power-Law Elliptic Section Bodies," AIAA Paper 2000-2553, 2000.

13 Grismer, M. J., Strang, W. Z., Tomaro, R. F., and Witzemman, F. C., "Cobalt: A Parallel, Implicit, Unstructured Euler/Navier- Stokes Solver," Advances in Engineering Software, Vol. 29, No. 3-6, 1998, pp. 365-373.

14 Fournier, E. Y., "Testing of the USAFA H3 Model in the DREV Tri Sonic Wind Tunnel," DREV-TN 2000-064, 2000.

15 Kittlye, RL, Packard, JD, Winchenbach, GL, "Description and Capabilities of the Aeroballistic Research Facility," AFATL-TR-87-08, May 1987

16 Winchenbach, GL, "Aerodynamic Testing In A Free-Flight Spark Range," WL-TR-1997-7006, April 1997

17 Fischer, MA and Hathaway, WH, "ARFDAS Users Manual," AFATL-TR-88-48, November 1988

18 Yates, LA, "A Comprehensive Aerodynamic Data Reduction System For Aeroballistic Ranges," WL-TR-96-7059, Wright Laboratory, Armament Directorate, Eglin AFB, FL, October 1996

19 Hathaway, WH and Whyte, RH, "Aeroballistic Research Facility Free Flight Data Analysis Using The Maximum Likelihood Method," AFATL-TR-79-98, Air Force Armament Laboratory, Eglin AFB, FL, December 1979

20 Murphy, CH, "Free Flight Motion of Symmetric Missiles," BRL Report 1216, Aberdeen Proving Ground, MD, July 1963

21 Murphy, CH "Data Reduction for the Free Flight Spark Ranges," BRL Report 900, Aberdeen Proving Ground, MD, February 1954

22 Moore, FG, McInville, RM, and Hymer, TC, "Review and Extension of Computational Methods for Noncircular Cross-Sectional Weapons," Journal of Spacecraft and Rockets, Vol. 35, No. 5, 1998, pp. 585-597

23 Moore, FG, McInville, RM, and Hymer, TC, "Application of the 1998 Version of the Aeroprediction Code," Journal of Spacecraft and Rockets, Vol. 36, No. 5, 1998, pp. 633-645

24 Moore, FG, private communication

25 Spalart, P. R. and Allmaras, S. R., "A One EquationTurbulence Model for Aerodynamic Flows," AIAA Paper 92-0439, Jan. 1992.

26 Baldwin, B. S. and Barth, T. J., "A One-Equation Turbulence Transport Model for High Reynolds Number Wall Bounded Flows," NASA-TM 102847, Aug. 1990.

27 Kennon, S. R., Meyering, J. M., Berry, C. W., and Oden, J. T., "Geometry Based Delaunay Tetrahedralization and Mesh Movement Strategies for Multi-Body CFD," AIAA Paper 92-4575, 1992.

28 Menter, FR, "Zonal Two Equation k-□ Turbulence Models for Aerodynamic Flows," AIAA 93-2906, 1993

29 Wilcox, DC, Turbulence Modeling for CFD, Second Edition, DCW Industries, Inc., 1998

30 Forsythe, JR, Strang, WZ, Hoffmann, KA, "Validation of Several Reynolds-Averaged Turbulence Models in a 3-D Unstructured Grid Code," AIAA 00-2552, June 2000

31 Pirzadeh, S, "Three-Dimensional Unstructured Viscous Grids by the Advancing-Layers Methods," AIAA Journal, Vol. 34, No. 1, 1996, pp. 257-265

32 http://www.va.afrl.af.mil/vaa/vaac/COBALT/

33 Schuricht, PH, Forsythe, JR, Bertin, JJ, and Abate, GL, "Comparison Between Measurements and Computations for Power-Law Elliptic Section Bodies," AIAA 00-2553, June 2000, Presented at Fluids 2000, Denver, CO

34 Urena, E. J. and Massett, A. P., "Shock Wave Analysis for a Power Law Elliptic (PLES) Section Configuration," USAFA project report for AE 471, 1999.

PAGE INTENTIONALLY LEFT BLANK

DISTRIBUTION

AFRL-MN-EG-TR-2001-7104

Defense Technical Information Center
8725 John J. Kingman Road, Suite 0944
Fort Belvoir, VA 22060-6218 1

NASA Langley Research Center
Technical Library Branch, MS 185
Attn: Document Cataloging
Hampton, VA 23665 1

Commander
Naval Weapons Center (Code 3431)
Attn: Technical Library
China Lake, CA 93555-6001 1

Commander
U.S. Army Research Laboratory
Attn: AMSRL-OP-CI-B (Tech. Lib.)
Aberdeen Proving Ground, MD 21005 1

Director
U.S. Army Research Laboratory
Attn: Dr. Peter Plostins
Aberdeen Proving Ground, MD 21005 3

Director
U.S. Army Research Laboratory
Attn: F Brandon
Aberdeen Proving Ground, MD 21005 1

Director
U.S. Army Research Laboratory
Attn: Dr. Ed Schmidt
Aberdeen Proving Ground, MD 21005 1

Commander
U.S. Army Armament Research Development and
Engineering Center
Attn: SMCAR-TDC
Picatinny Arsenal, NJ 07806 1

Commander
U.S. Army Armament Research Development and
Engineering Center
Attn: AMSTA-AR-AET-A
Picatinny Arsenal, NJ 07806 1

Air University Library
600 Chennault Circle, Bldg 1405
Maxwell AFB, AL 36112-6424 1

United States Air Force Academy
Department of Aeronautics
ATTN: John Bertin
USAFA, CO 80840 5

Commander
U.S. Army Armament Research Development and
Engineering Center
Attn: AMSTA-AR-CCH-B
Picatinny Arsenal, NJ 07806 1

Commander
U.S. Army Armament Research Development and
Engineering Center
Attn: AMSTA-AR-FSE
Picatinny Arsenal, NJ 07806 1

Commander
U.S. Army Armament Research Development and
Engineering Center
Attn: AMSTA-AR-CCL-B
Picatinny Arsenal, NJ 07806 1

Commander
U.S. Army Armament Research Development and
Engineering Center
Attn: AMSTA-AR-CCH-A
Picatinny Arsenal, NJ 07806 1

Director
U.S. Army Research Office
PO Box 12211
Research Triangle Park, NC 27709-2211 1

Director
U.S. Army Benet Laboratory
Attn: SMCAR-CCB-R
Watervaliet, NY 12189 1

Director
U.S. Belvior Research Development and
Engineering Center
Attn: SATBE-FED
Ft. Belvior, VA 22060 1

Eglin AFB Offices:
AFRL/MN CA-N 1
AFRL/MNAV 10
AFRL / MNOC-1 (STINFO Office) 1

Arrow Tech Associates
1233 Shelburne Road, Suite D-8
South Burlington, Vermont 05403 2

Aeroprediction Incorporated
9449 Grover Drive, Suite 201
King George, VA 22485 2